Cell Reports
Medicine

Article

Microcircuit failure in *STXBP1* encephalopathy leads to hyperexcitability

Graphical abstract

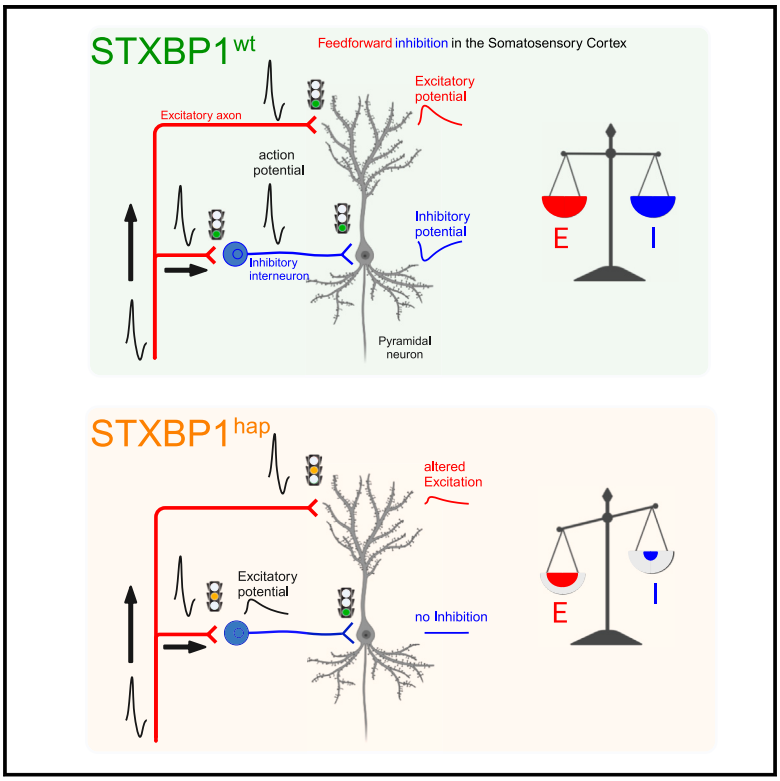

Authors

Altair Brito dos Santos, Silas Dalum Larsen, Liangchen Guo, ..., Matthijs Verhage, Jakob Balslev Sørensen, Jean-François Perrier

Correspondence

perrier@sund.ku.dk

In brief

Stxbp1 haploinsufficiency is associated with cortical hyperexcitability. Brito dos Santos et al. report that in an *Stxbp1* model, excitatory synapses are selectively impaired. This leads to a failure to recruit inhibitory parvalbumin-positive interneurons within feedforward inhibition microcircuits, leading to hyperexcitability at the level of pyramidal neurons.

Highlights

- Neocortical microcircuits fail in an *Stxbp1* haploinsufficiency model (*Stxbp1*^{hap})
- Lack of feedforward inhibition leads to cortical hyperexcitability
- Inhibitory synapses are unaffected but excitatory synapses fail to recruit interneurons
- Ampakines rescue microcircuit failure in *Stxbp1*^{hap}

dos Santos et al., 2023, Cell Reports Medicine *4*, 101308
December 19, 2023
https://doi.org/10.1016/j.xcrm.2023.101308

CellPress

Cell Reports Medicine

CellPress
OPEN ACCESS

Article

Microcircuit failure in *STXBP1* encephalopathy leads to hyperexcitability

Altair Brito dos Santos,[1] Silas Dalum Larsen,[1] Liangchen Guo,[1] Paola Barbagallo,[1] Alexia Montalant,[1] Matthijs Verhage,[2,3] Jakob Balslev Sørensen,[1] and Jean-François Perrier[1,4,*]

[1]Department of Neuroscience, University of Copenhagen, Blegdamsvej 3, 2200 Copenhagen N, Denmark

[2]Department of Functional Genomics, Center for Neurogenomics and Cognitive Research (CNCR), Vrije Universiteit Amsterdam and Amsterdam University Medical Center, De Boelelaan 1085, 1081 HV Amsterdam, the Netherlands

[3]Department of Human Genetics, Center for Neurogenomics and Cognitive Research (CNCR), Vrije Universiteit Amsterdam and Amsterdam University Medical Center, De Boelelaan 1085, 1081 HV Amsterdam, the Netherlands

[4]Lead contact

*Correspondence: perrier@sund.ku.dk

https://doi.org/10.1016/j.xcrm.2023.101308

SUMMARY

De novo mutations in *STXBP1* are among the most prevalent causes of neurodevelopmental disorders and lead to haploinsufficiency, cortical hyperexcitability, epilepsy, and other symptoms in people with mutations. Given that Munc18-1, the protein encoded by *STXBP1*, is essential for excitatory and inhibitory synaptic transmission, it is currently not understood why mutations cause hyperexcitability. We find that overall inhibition in canonical feedforward microcircuits is defective in a P15-22 mouse model for *Stxbp1* haploinsufficiency. Unexpectedly, we find that inhibitory synapses formed by parvalbumin-positive interneurons were largely unaffected. Instead, excitatory synapses fail to recruit inhibitory interneurons. Modeling confirms that defects in the recruitment of inhibitory neurons cause hyperexcitation. CX516, an ampakine that enhances excitatory synapses, restores interneuron recruitment and prevents hyperexcitability. These findings establish deficits in excitatory synapses in microcircuits as a key underlying mechanism for cortical hyperexcitability in a mouse model of *Stxbp1* disorder and identify compounds enhancing excitation as a direction for therapy.

INTRODUCTION

Neurodevelopmental disorders include syndromes with frequent epileptic episodes, which often are refractory to medication. Because epilepsy can be triggered experimentally by blocking inhibitory synaptic or voltage-gated conductances or by activating excitatory conductances, it is widely assumed that a change in the ratio of excitation and inhibition underlies epileptic states. For instance, a frequent cause of the severe Dravet syndrome is loss-of-function mutations in the *SCN1A* gene, which encodes a voltage-gated sodium channel, $Na_v1.1$, that supports action potential generation specifically in inhibitory interneurons.[1] However, with the advent of routine genetic testing of children with epilepsies, it has become clear that mutations also occur in genes that are equally involved in excitatory and inhibitory mechanisms.[2,3] One prominent example is *STXBP1*. *STXBP1* encodes the protein Munc18-1, which organizes SNARE-complex formation.[4,5] The SNARE-complex drives the exocytosis of neurotransmitter-filled vesicles in all synapses and thereby underlies all of the chemical synaptic transmission in the brain; in the absence of Munc18-1, neurotransmission is arrested.[6] *STXBP1* encephalopathy, caused by heterozygous mutation, is typically characterized by epilepsy, cortical hyperexcitability, intellectual disability, movement disorders, and often autism.[7–9]

Among the mutations leading to *STXBP1* encephalopathy are truncations, microdeletions, and missense mutations.[7] Missense mutations lead to protein instability.[10–14] Accordingly, the main molecular hypothesis is that haploinsufficiency causes the syndrome.[15] This is conveniently modeled in mice by removing one allele (*Stxbp1*$^{+/-}$), which reduces *STXBP1* expression to half.[16] Indeed, like human patients, this mouse model displays frequent epileptic episodes with spike-wave discharges as well as diffuse hyperexcitability in most brain areas, anxiety, cognitive deficits, and behavioral inflexibility.[11] These results were confirmed in different models of *Stxbp1* haploinsufficiency.[17–19]

Defects in synaptic transmission have been identified in cultured neurons[16,20] and in brain slices[18,19] of *Stxbp1*$^{+/-}$ mice, as well as in human neurons derived from engineered *Stxbp1*$^{+/-}$ embryonic stem cells.[21] STXBP1 missense mutations expressed in *Stxbp1* null mouse neurons give rise to synaptic phenotypes in some, but not all, cases.[11] However, until now, experiments have only considered single synapse types studied in isolation (and most often in cultured neurons) without taking into account the circuitry in which they are normally embedded.

How can mutations in genes involved in both excitatory and inhibitory synapses result in hyperexcitability/epilepsy? One crucial aspect to consider is the exact way in which excitatory and inhibitory neurons interact within microcircuits[22,23]—in other

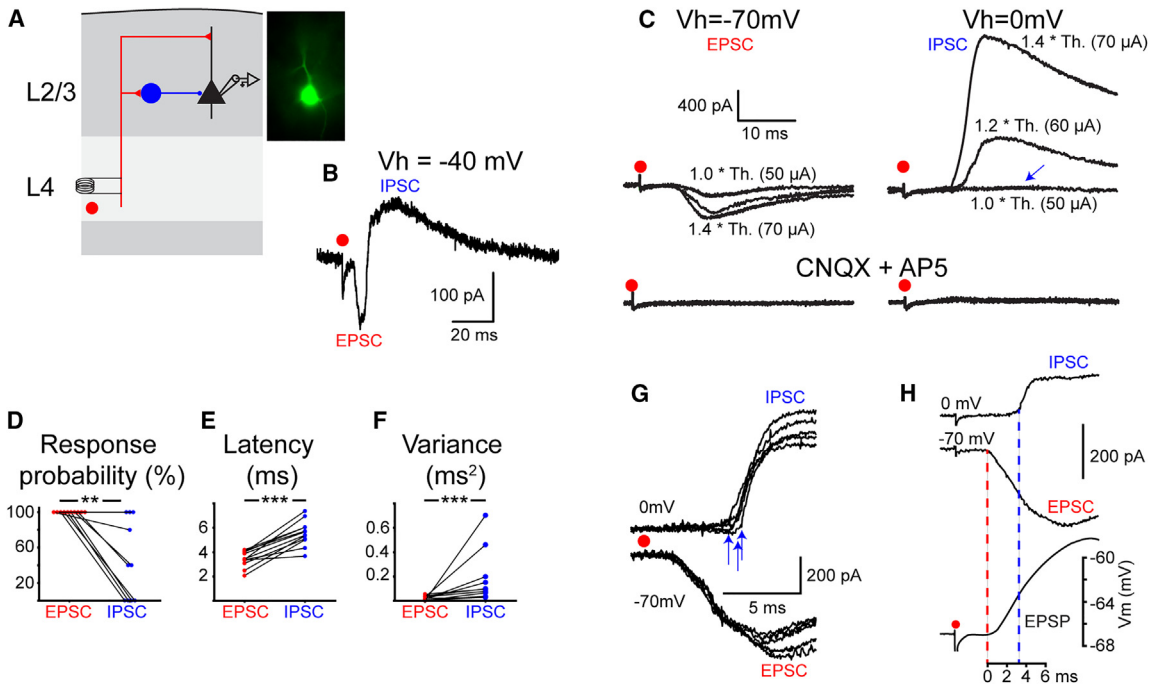

Figure 1. Characterization of feedforward microcircuits in WT (*Stxbp1*^{wt}) animals

(A) Schema of the experimental protocol. L4 excitatory input stimulated with a bipolar electrode. L2/L3 pyramidal cell recorded with whole-cell patch-clamp technique. Blue: inhibitory interneuron. Image: Epifluorescence photograph of a patched pyramidal neuron.

(B) Voltage-clamp recording of an L2/3 pyramidal cell of the somatosensory cortex in response to a single stimulation applied in L4 at 1.4 × threshold. V_h = −40 mV. Average of 5 sweeps. An EPSC was followed by an IPSC (n = 7).

(C) Voltage-clamp recording of an L2/3 pyramidal cell from the somatosensory cortex in response to single shocks of increasing intensities applied in L4. EPSCs and IPSCs isolated by holding the potential at −70 and 0 mV. Stimulation at threshold (50 µA) evoked an EPSC but no IPSC (arrow). After bath application of the glutamate receptor antagonists CNQX (15 µM) and AP5 (50 µM) EPSCs and IPSCs were abolished (n = 3). Th., threshold.

(D) Fraction of EPSCs and IPSCs evoked by L4 stimulation at the threshold (i.e., the stimulation intensity that induces EPSCs 5 of 5 times; n = 10) (IPSCs occurred in 46% ± 14.3% of recordings; p = 0.003).

(E) Mean latencies of EPSCs and IPSCs evoked by L4 stimulations. Significant difference (mean latency for EPSCs 3.4 ± 0.2 ms, IPSCs 5.5 ± 0.3 ms; p = 0.0005, n = 12).

(F) Variance of the latencies of EPSCs and IPSCs. Significant difference (mean variance for EPSC latencies 0.018 ± 0.005 ms^2, IPSCs 0.14 ± 0.06 ms^2; p = 0.0005, n = 12).

(G) EPSCs and IPSCs evoked by 1.4 × threshold (70 µA) L4 stimulations (5 superimposed traces). EPSCs occurred at almost fixed latency, but the delay of IPSCs was variable (arrows).

(H) Superimposed voltage-clamp (Vh = 0 and −70 mV) and current clamp responses of a pyramidal cell to a single shock in L4. The IPSC starts 3 ms after the EPSC (i.e., in the middle of the ascending phase of the EPSP).

words, small circuits with stereotypical interconnections, which carry out basic computation tasks in the brain. The feedforward inhibition (FFI) microcircuit is crucially important for information processing in many brain areas (Figure 1A).[22,24] In the cortex, layer 4 (L4) serves as the input layer for thalamocortical afferents carrying sensory information. An excitatory (glutamatergic) axon projects from L4 to L2/3 to stimulate a glutamatergic pyramidal neuron, whereas an axonal branch stimulates an inhibitory (GABAergic) parvalbumin-positive (PV$^+$) interneuron, which in turn forms an inhibitory synapse on the pyramidal output neuron. Upon stimulation of this three-synapse microcircuit, a brief excitatory potential (EPSP) stimulates the pyramidal neuron before arrival of the inhibitory potential (IPSP) from the PV$^+$ neuron. Summation of several inputs during the short time window between the EPSP and the IPSP represents the computational task of the microcircuit.[25] By balancing excitatory and inhibitory drives to the L2/3 pyramidal neuron, the FFI microcircuit can be driven at high frequencies without compromising the excitation/inhibition (E/I) ratio.

Here, we set out to understand the role of FFI in *STXBP1* encephalopathy by recording excitatory and inhibitory synaptic responses in L2/3 of the mouse somatosensory cortex using a heterozygous mouse model for *STXBP1* encephalopathy.[11] Our results show that excitatory, not inhibitory, synapses of the microcircuit are strongly impaired by the mutation. The inability of excitatory synapses to recruit PV$^+$ interneurons induces an alteration of the E/I ratio. We demonstrate that this change leads to hyperexcitability of principal neurons when input is distributed between different afferents and that hyperexcitability can be reverted by strengthening glutamatergic synapses using a positive allosteric modulator for α-amino-3-hydroxy-5-methyl-4-isoxazolepropionic acid (AMPA) receptors (an ampakine), pointing to a novel treatment principle.

RESULTS

FFI microcircuit in wild-type (WT) *Stxbp1*^{wt} animals

We monitored FFI microcircuits in L2/3 of the mouse somatosensory cortex, starting with WT (*Stxbp1*^{wt}) animals. Additional experiments were carried out in the motor cortex and in the dentate gyrus and CA1 region of the hippocampus. The stimulation of cortical L4 excitatory inputs resulted in a monosynaptic excitatory postsynaptic current (EPSC) followed by a disynaptic inhibitory postsynaptic current (IPSC) in L2/3 cortical neurons (Figures 1A and 1B). The stimulation intensity was adjusted to a threshold that would elicit EPSCs in 5 of 5 trials in the recorded pyramidal cell.[24] We isolated EPSC and IPSC by clamping to different voltages (EPSCs were measured at −70 mV and IPSCs at 0 mV). The threshold for IPSCs was higher than it was for EPSCs (Figures 1C and 1D). EPSCs occurred at almost fixed latencies, whereas IPSCs showed millisecond variability in their delay (jitter) (Figures 1E–1G). Moreover, blocking excitatory ionotropic receptors (CNQX and AP5) abolished both excitatory and inhibitory responses (Figure 1C), establishing the disynaptic nature of the IPSC. More important, L4-evoked EPSPs had a rise time that exceeded the latency of the inhibitory postsynaptic signal (Figure 1H), indicating significant overlap between excitatory and inhibitory components, such that the amplitude of the resulting EPSPs strongly depends on the degree of recruitment of inhibitory synapses in the feedforward inhibitory microcircuit. These results establish that the stimulation induced the synaptic activation of a GABAergic interneuron mediating FFI.[24–26]

FFI is altered in *Stxbp1*^{hap} animals

Next, we compared *Stxbp1*^{wt} to *Stxbp1* heterozygous littermates, leading to 50% reduced Stxbp1 expression (Figures S1A and S1B). Previous data showed that similar to other models,[17–19] the mouse we used in this study constitutes a valid model for *STXBP1* haploinsufficiency[11] and is therefore referred to as *Stxbp1*^{hap} forward. To investigate the excitatory and inhibitory inputs to L2/3 pyramidal neurons, we again isolated EPSCs and IPSCs by clamping to different voltages (EPSCs were measured at −70 mV and IPSCs at 0 mV). Upon stimulation at L4, both EPSCs and IPSCs were significantly smaller in *Stxbp1*^{hap} microcircuits (Figure 2B). This difference was significant for stimulation applied at ≥1.2× threshold (Figure 2C). When the stimulation was adjusted to the minimal intensity that produced at least one EPSC and failures otherwise during 10 consecutive trials (Figure S1C), we found that the synaptic potency (mean amplitude of successful responses) was not affected by the mutation. By contrast, the synaptic efficacy (mean amplitude of all of the responses, including failures) was reduced because of a decrease in the probability of release (ratio between number of successes and total number of stimuli) (Figure S1D). The amplitudes of spontaneously occurring mEPSCs and mIPSCs recorded in the presence of tetrodotoxin (1 μM) were not affected by the mutation (Figures S1E–S1G). The frequencies of mEPSCs were decreased, as was observed in neurons from humans and invertebrates.[21,27] We also noticed a slight reduction in the frequencies of mIPSCs, even though the difference was not significant in our sample (Figure S1G). These data confirm that synaptic transmission is impaired in *Stxbp1*^{hap} microcircuits. For this reason, reaching the threshold for action potentials in postsynaptic neurons may require stronger stimulations in mutant animals. To avoid this bias, we also plotted the amplitude of synaptic responses as a function of the absolute stimulation intensity (in μA). Again, the amplitudes of EPSCs and IPSCs were significantly lower in *Stxbp1*^{hap} microcircuits (Figure 2D). It is important to note that we found similar alterations of FFI microcircuits in the motor cortex and in the dentate gyrus and CA1 region of the hippocampus (Figures S1H–S1K). Hence, for different microcircuits in distinct brain areas, excitatory inputs trigger impaired responses in *Stxbp1*^{hap} FFI microcircuits.

Because both excitatory and inhibitory transmission onto the L2/3 pyramidal neurons were reduced in the *Stxbp1*^{hap}, the consequences for overall inhibition within the microcircuit was not immediately clear. To dissect the deficiency, we first quantified the number of PV$^+$ neurons in L2/3 and found no significant difference between *Stxbp1*^{wt} and *Stxbp1*^{hap} animals (Figures S1L and S1M) as reported previously in a different mouse model of *Stxbp1* haploinsufficiency.[19] We then stepped the holding voltage in the pyramidal neuron during stimulation, allowing us to estimate the total (inhibitory and excitatory) synaptic conductance (G_{syn}) and the reversal potential of synaptic currents, by linear regression in a current-voltage (I-V) plot (Figure 2E – inset). As expected, G_{syn} was much smaller in *Stxbp1*^{hap} synapses (Figures 2E–2G). In *Stxbp1*^{wt} microcircuits, the reversal potential (E_{rev}) of synaptic responses reached negative values (−43 ± 2 mV) near the reversal potential for chloride (calculated as −68 mV) (Figures 2E and 2H), suggesting that the response was dominated by inhibition, in agreement with previous findings.[24,28] By contrast, in *Stxbp1*^{hap} microcircuits, the values of E_{rev} were more scattered and remained closer to the reversal potential for excitation (−23 ± 8 mV; Figures 2F and 2H). These data demonstrate that in *Stxbp1*^{hap} microcircuits, FFI is impaired and that, consequently, overall inhibition is reduced (see also calculations of E/I ratio below).

Inhibitory synapses are not impaired in *STXBP1*^{hap} microcircuits

To dissect the function of each synapse in the FFI microcircuit directly, double recordings of connected neurons are necessary. To that end, we created *Stxbp1*^{hap} mice expressing Cre under control of the PV− promoter and crossed them with a conditional Salsa6f mouse line, which results in the expression of a fluorescent marker (tdTomato) in PV$^+$ cells in *Stxbp1*^{hap} and control littermates (Figure S2). Using the fluorescent marker as a guide, we performed simultaneous patch clamp recordings of L2/3 PV$^+$ interneurons and connected L2/3 pyramidal neurons (Figures 3A–3C). Single-action potentials evoked by brief depolarizing current pulses in PV$^+$ cells induced unitary IPSCs in pyramidal neurons. It is surprising that neither the latency nor the slope were affected by reduced *Stxbp1* expression (Figure 3D). The amplitude was slightly larger, although not significantly larger (Figure 3D). This could suggest a compensatory mechanism that is specific for inhibitory synapses that was not investigated further. The synaptic conductance was not different (Figures 3E–3G), and the reversal potential for inhibition (E_i) had similar values for both genotypes (Figures 3H). These data

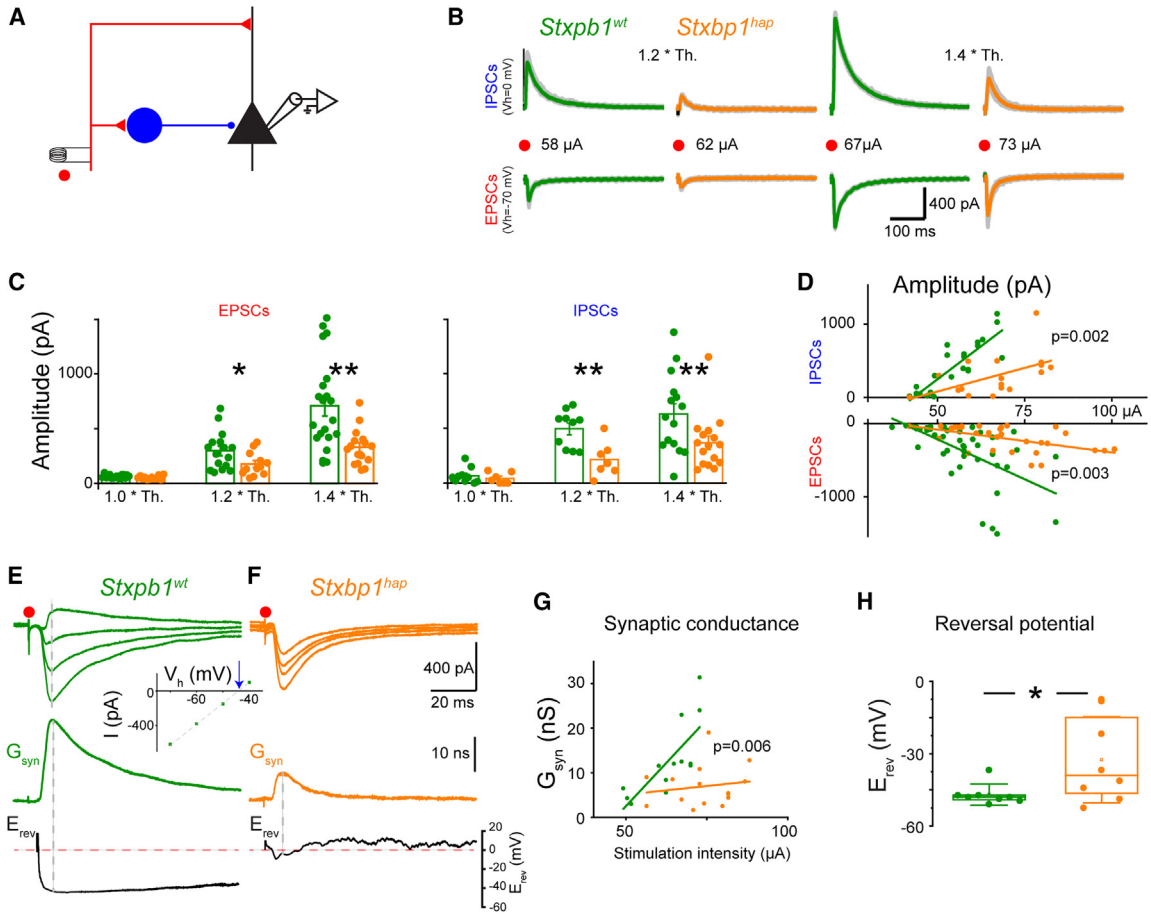

Figure 2. Feedforward microcircuits from the somatosensory cortex are altered in *Stxbp1*^{hap} animals

(A) Schema of the experimental protocol.

(B) EPSCs (V_h = −70 mV) and IPSCs (V_h = 0 mV) evoked in L2/3 pyramidal cells from the somatosensory cortex of *Stxbp1*^{wt} and *Stxbp1*^{hap} animals. Six superimposed sweeps. Color traces: average of all of the sweeps.

(C) Amplitudes of EPSCs and IPSCs were higher in *Stxbp1*^{wt} than in *Stxbp1*^{hap} animals. Th., threshold for EPSC. Mean amplitude of EPSCs ± SEM at 1.0 Th.: −62 ± 4.0, n = 16 versus −51 ± 5 pA, n = 12, p = 0.11; IPSCs at 1.0 Th.: 66 ± 22, n = 10 versus 42 ± 19 pA, n = 7, p = 0.48; amplitude of EPSCs at 1.2 Th.: −298 ± 43, n = 16 versus −175 ± 31 pA, n = 12, p = 0.03; IPSCs at 1.2 Th.: 495 ± 53, n = 10 versus 214 ± 60 pA, n = 7, p = 0.003; amplitude of EPSCs at 1.4 Th.: −657 ± 78, n = 26 versus −351 ± 34 pA, n = 21, p = 0.002; IPSCs at 1.4 Th.: 633 ± 94, n = 15 versus 367 ± 63 pA, n = 16, p = 0.003. *p < 0.05; **p < 0.01.

(D) Amplitudes of EPSCs and IPSCs plotted as function of stimulation intensity. Slopes for EPSCs −21.8 ± 4.6 pA/µA (n = 44) versus −6.2 ± 1.8 pA/µA (n = 30), p = 0.003, F test; slopes for IPSCs 36.0 ± 4.4 pA/µA (n = 30) versus 12.9 ± 5.4 pA/µA (n = 20), p = 0.002, F test.

(E) Upper traces: voltage-clamp recording of an L2/3 pyramidal cell of the somatosensory cortex in response to a single stimulation applied in L4 from an *Stxbp1*^{wt} animal. V_h = −70, −60, −50, and −40 mV. Each trace is an average of 5 sweeps. Inset: I-V plot obtained at the time of the dashed line illustrating the linear relationship between current and voltage. R^2 = 0.99. Middle trace: G_{syn} calculated as the slope of the I-V plot for each time point. Lower trace: E_{rev} of the synaptic response calculated as the x intercept of each I-V plot (arrow in the inset).

(F) Similar results as in (E) from an *Stxbp1*^{hap} animal. Adjacent averaging filter (20-point window) applied on the E_{rev} trace.

(G) G_{syn} as function of stimulation intensity (*Stxbp1*^{wt}: 0.77 ± 0.20 nS/µA, n = 13; *Stxbp1*^{hap} 0.08 ± 0.13 nS/µA, n = 15; p = 0.006, F test).

(H) E_{rev} at the time corresponding to the peak of G_{syn} (*Stxbp1*^{wt}: −42.8 ± 2.1 mV, n = 8; *Stxbp1*^{hap}: −23.5 ± 8.4 mV, n = 8; p = 0.04). *p < 0.05.

demonstrate that, unexpectedly, the inhibitory synapses on the pyramidal cells are unaffected by reduced *Stxbp1* expression, at least upon single-action potentials induced in PV$^+$ cells.

Excitatory synapses are impaired in *Stxbp1*^{hap} microcircuits

Because net inhibition in the FFI microcircuit was clearly impaired in *Stxbp1*^{hap} microcircuits (Figure 2, see also below), although the inhibitory synapse between PV$^+$ neurons and pyramidal neurons was unaffected, we hypothesized that the excitatory synapse between L4 and PV$^+$ cells is defective, leading to a failure to recruit PV$^+$ neurons, as seen in the caudate putamen.[18] We tested this hypothesis by recording PV$^+$ interneurons in current-clamp mode in response to L4 stimulation. Note that in these experiments, a second patch-clamp electrode in the L2/3 pyramidal neurons (not shown in Figure 4A) was used to set the stimulation threshold value, which, as before, was the stimulation intensity that elicited EPSCs in 5 of 5 trials in the recorded pyramidal cell. At the threshold, action potentials were mostly present in PV$^+$ neurons from *Stxbp1*^{wt} animals but mostly absent

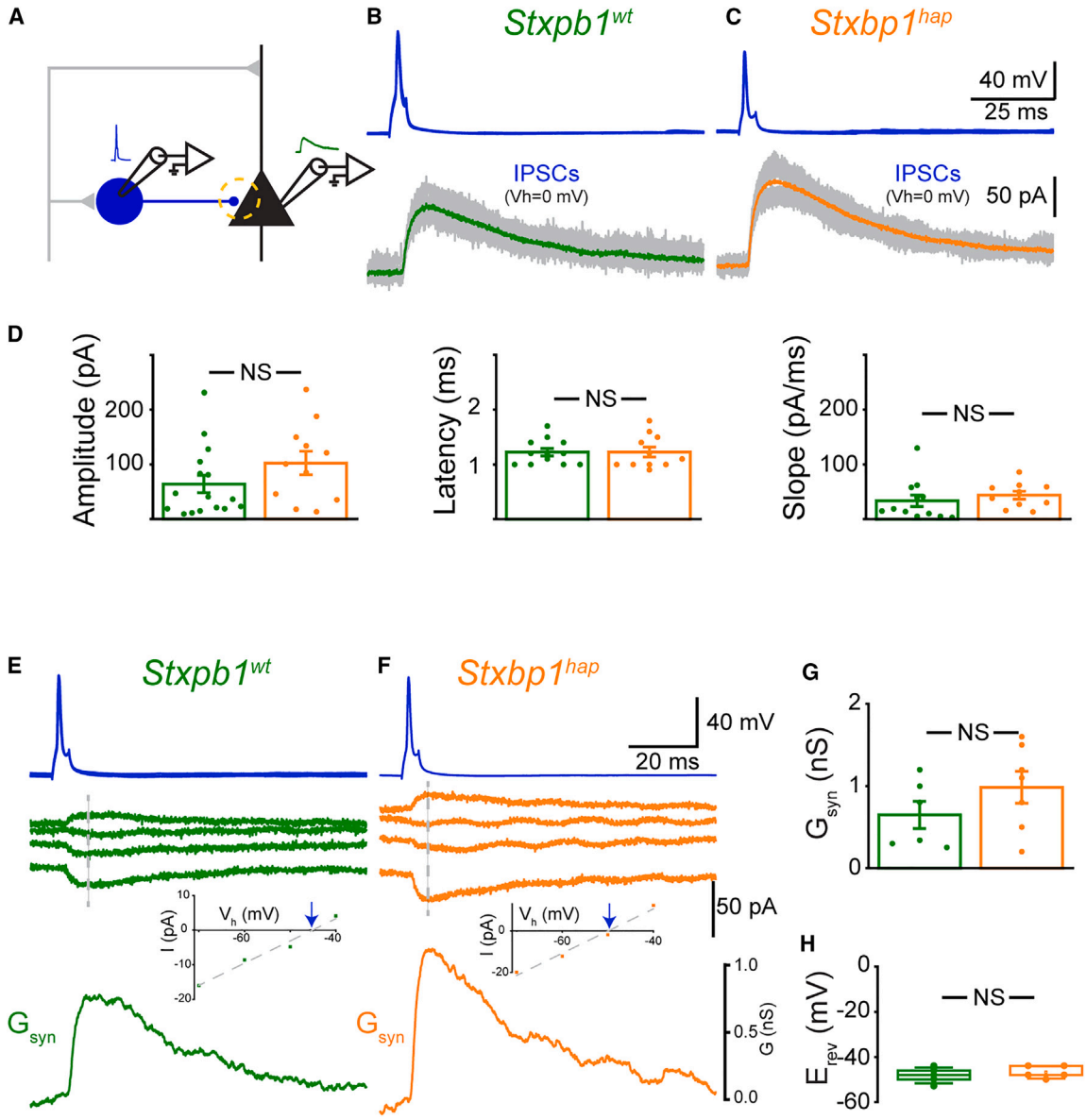

Figure 3. Inhibitory synapses are not impaired in the somatosensory cortex of *Stxbp1*^{hap} animals

(A) Schema of the experimental protocol.

(B) Simultaneous recording of a PV^{+} neuron and of a connected L2/3 pyramidal cell of the somatosensory cortex from an *Stxbp1*^{wt} animal. PV^{+} neuron recorded in current clamp. Each action potential induced in PV^{+} neurons evoked an IPSC in the pyramidal cell (V_h = 0 mV). Gray: 10 consecutive traces. Green: average. Inset: schema of the experimental protocol.

(C) Similar results as in (B) obtained from an *Stxbp1*^{hap} animal.

(D) Mean amplitudes ± SEM, latencies, and slopes of IPSCs evoked by one action potential in *Stxbp1*^{wt} and in *Stxbp1*^{hap} animals. Amplitudes, 64.1 ± 15.8 pA (n = 16) versus 102.5 ± 21.8 pA (n = 11), p = 0.16; latencies: 1.1 ± 0.1 ms (n = 12) versus 1.2 ± 0.1 ms (n = 11), p = 0.93; slope: 33.4 ± 10.6 pA/ms (n = 12) versus 43.8 ± 7.3 pA/ms (n = 10), p = 0.18. NS, nonsignificant.

(E) Upper traces simultaneous recording of a PV^{+} neuron and of a connected L2/3 pyramidal cell of the somatosensory cortex from an *Stxbp1*^{wt} animal. PV^{+} neuron recorded in current clamp. Pyramidal neuron recorded in voltage-clamp mode at V_h = −40, −50, −60, and −70 mV. Each trace is the average of 5 consecutive sweeps. Inset: I-V plot obtained at the time marked by the dashed line. The x intercept indicates the reversal potential of the IPSC. Lower trace: G_{syn} calculated as the slope of the I-V plot for each time point.

(F) Similar results as in (E) obtained from an *Stxbp1*^{hap} animal.

(G) Mean maximal amplitude ± SEM of G_{syn} for the 2 genotypes. Similar G_{syn} in *Stxbp1*^{hap} and *Stxbp1*^{wt} animals (mean amplitude in *Stxbp1*^{wt}: 0.64 ± 0.17 nS, n = 6 and in *Stxbp1*^{hap} animals: 0.99 ± 1.2 nS, n = 7, p = 0.28). NS, nonsignificant.

(H) E_{rev} at the time corresponding to the peak of G_{syn} (*Stxbp1*^{wt}: −48.0 ± 1.6 mV, n = 5; *Stxbp1*^{hap}: −47.0 ± 1.2 mV, n = 5; p = 0.64). NS, nonsignificant.

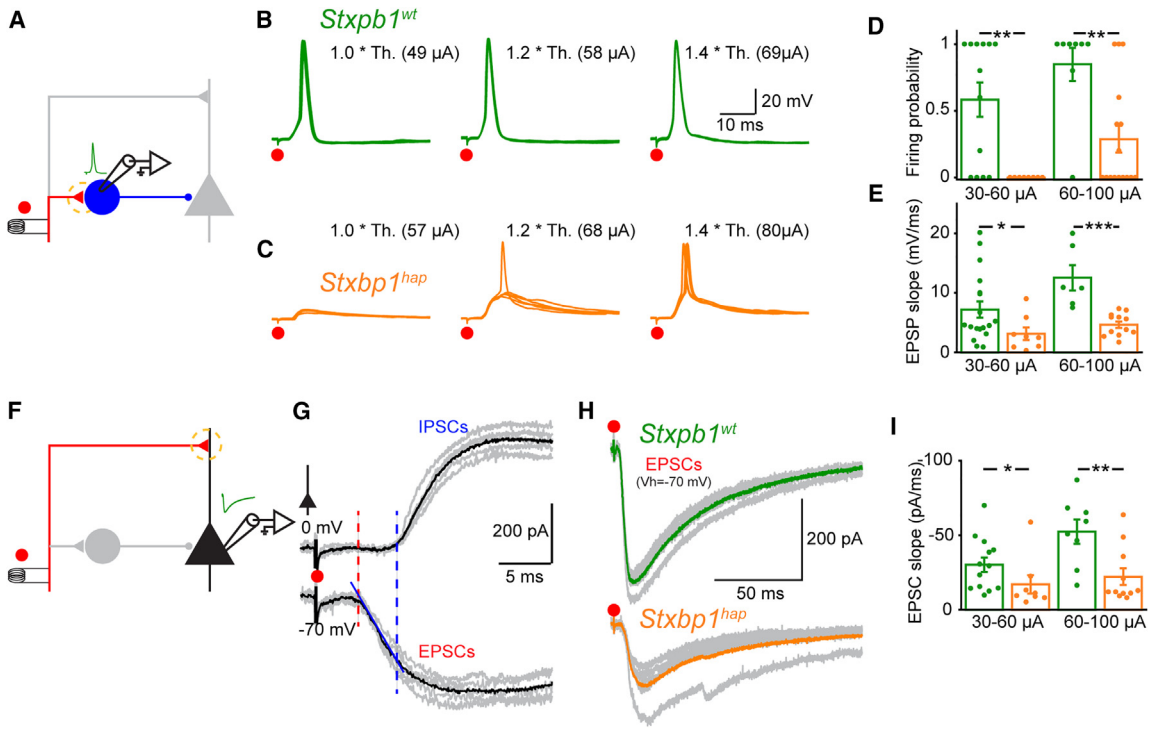

Figure 4. Excitatory synapses from the somatosensory cortex of *Stxbp1*^{hap} animals are impaired

(A) Schema of the experimental protocol.

(B) Membrane potential of an L2/3 PV^{+} interneuron from an *Stxbp1*^{wt} animal in response to a single shock applied on L4 at increasing intensities. The threshold (Th.) is the lowest stimulation intensity that produces 5 EPSCs in pyramidal neurons without failure (see STAR Methods).

(C) Same display as in (B) obtained from an *Stxbp1*^{hap} animal. The PV^{+} cell is less excitable compared to *Stxbp1*^{wt} animals.

(D) Mean firing probability ± SEM of PV^{+} cells lower in *Stxbp1*^{hap} animals. Each dot corresponds to the average of 5 consecutive sweeps (30–60 µA: 0.58 ± 0.13 [n = 13] versus 0.00 ± 0.00 [n = 8], p = 0.004; 60–100 µA: 0.85 ± 0.12 [n = 8] versus 0.29 ± 0.10 [n = 16], p = 0.008). **p < 0.01.

(E) Mean EPSP slopes ± SEM smaller in *Stxbp1*^{hap} animals. Each dot corresponds to the average of 5 consecutive sweeps (30–60 µA: 7.2 ± 1.4 [n = 18] versus 3.1 ± 1.0 mV/ms [n = 8], p = 0.04; 60–100 µA: 12.6 ± 2.1 [n = 6] versus 4.7 ± 0.55 mV/ms [n = 12], p = 0.0001). *p < 0.05; ***p > 0.001

(F) Schema of the experimental protocol.

(G) Voltage-clamp recording of an L2/3 pyramidal cell in response to L4 stimulation at 56 µA. Gray: individual traces. Black: average of 5 consecutive sweeps. IPSCs started 2.5 ms after EPSCs. Red: EPSC slope before the start of IPSC.

(H) Examples of EPSCs from *Stxbp1*^{wt} and *Stxbp1*^{hap} animals.

(I) Mean EPSC slopes ± SEM smaller in *Stxbp1*^{hap} animals (30–60 µA: −30.2 ± 5.0 [n = 13] versus −17.1 ± 6.2 pA/ms [n = 8], p = 0.02; 60–100 µA: −52.4 ± 8.1 [n = 8] versus −22.2 ± 5.7 pA/ms [n = 11], p = 0.005). *p < 0.05; **p < 0.01.

in *Stxbp1*^{hap} animals (Figures 4B and 4C). We plotted the firing probability and the synaptic strength, estimated by EPSP slope, as a function of the absolute stimulation intensity (Figures 4D and 4E). For all of the intensities tested, the slope of EPSPs in the PV^{+} cells and the firing probability were strongly reduced in *Stxbp1*^{hap} microcircuits (Figures 4D and 4E). This difference was also significant when comparing the EPSP slopes as a function of threshold for EPSCs in pyramidal neurons (Figures S3A and S3B) or when comparing the amplitude of EPSCs evoked in PV cells (Figures S3C and S3D). This result confirms that the deficit of inhibition observed in mutant animals is caused by the impairment of the excitatory synapses formed on PV^{+} interneurons. We also noticed that the amplitude of action potentials evoked in PV cells was smaller in *Stxbp1*^{hap} animals (*Stxbp1*^{wt}: 80 ± 1.8 mV, n = 62; *Stxbp1*^{hap}: 66 ± 1.6 mV; n = 25; p < 0.0001).

To estimate the strength of the other excitatory synapse of the FFI microcircuit (i.e., between L4 and L2/3 pyramidal neurons), we recorded the response of pyramidal cells to L4 stimulation (Figure 4F). By holding the membrane potential at −70 and 0 mV, we observed that IPSCs started 2.5 ms after the beginning of EPSCs (Figure 4G). This difference was similar for both genotypes (*Stxbp1*^{wt}: 2.7 ± 0.3 ms; *Stxbp1*^{hap}: 2.3 ± 0.4 ms; n = 7 for each genotype; p = 0.59). The slope of the first 2 ms of the EPSC is therefore a good proxy for estimating the strength of the excitatory synapse. As for the L4-PV^{+} synapse, we found that EPSCs in *Stxbp1*^{hap} microcircuits were weaker than in control microcircuits (Figures 4H and 4I). This difference was also significant when comparing the slopes as a function of threshold for EPSCs in pyramidal neurons (Figures S3H and S3I). To validate these results, we measured the synaptic strength of the three synapses within the same FFI microcircuits by performing simultaneous patch-clamp recording of PV^{+} and connected pyramidal cells in response to single stimuli applied at L4 and to evoked action potentials in PV^{+} neurons (Figure S4). Here again, we found that the net inhibition of pyramidal cells was deficient in *Stxbp1*^{hap} microcircuits (Figures S4B–S4D) because of

the inability of excitatory synapses to recruit PV^+ interneurons (Figures S4I–S4M), although inhibitory synapses were apparently not affected by reduced STXBP1 expression (Figures S4E–S4H). To quantify the impairment of the microcircuit, we compared the amplitude of L4-induced IPSCs with IPSCs evoked by one action potential in one PV cell. We found that the mean ratio of L4 to single PV cell–evoked IPSCs had a value of 21 ± 15 in in *Stxbp1*^{WT} and 6 ± 4 in *Stxbp1*^{hap}, suggesting that 3 to 4 times fewer PV^+ cells were recruited in mutant animals. Taken together, these data indicate that the functional impairments observed in *Stxbp1*^{hap} microcircuits in response to single stimuli are explained by deficiencies in the excitatory synapses.

The ratio between excitation and inhibition is altered in *Stxbp1*^{hap}

Next, we quantified the overall ratio between excitation and inhibition of the microcircuit by measuring the relative contribution of G_e and G_i to G_{syn} in pyramidal cells. This was possible because in the experiments above (Figure 3H), we directly identified the reversal potential for inhibition (E_i = −48 mV) (see STAR Methods). To validate the procedure, we calculated the contribution of G_e and G_i induced in pyramidal cells in response to one spike evoked in PV^+ neurons. As expected for an inhibitory synapse, G_i was identical to G_{syn}, and G_e remained at zero (Figure S5). In *Stxbp1*^{wt} microcircuits, G_e increased rapidly and was immediately followed by a larger G_i (Figures 5A and 5E), in agreement with previous work.[24,28] The relative fraction of G_e to G_{syn} decreased rapidly during synaptic transmission, whereas the fraction of G_i dominated (Figures 5B and 5F). As a result, the E/I ratio remained below 1 (Figure 5G). In *Stxbp1*^{hap} animals, the relative amplitude of G_i compared to G_e was much smaller than in control animals, excitation dominated (Figures 5D–5F), and the E/I ratio was considerably larger (Figure 5G). These data demonstrate that the lack of functional inhibition caused by the weakness of excitatory inputs on PV^+ interneurons results in a large alteration of the E/I ratio at the level of the pyramidal neuron that favors excitation.

Faster rundown of excitatory and inhibitory synapses in *Stxbp*^{hap} reduces the recruitment of PV^+ interneurons

Next, we investigated how reduced *Stxbp1* expression affected feedforward microcircuits during repetitive firing. Synaptic responses evoked in L2/L3 pyramidal cells by 10 stimuli at 10 Hz given to L4 afferents decreased slightly in *Stxbp1*^{wt} animals (Figures 5H and 5I). G_{syn} was dominated by inhibition (Figures 5H, 5J, and 5K). In *Stxbp1*^{hap} animals, the decrease in G_{syn} was more pronounced due to a strong reduction in G_i that almost disappeared by the end of the simulation train (Figures 5H and 5I; note that Figure 5I displays the degree of rundown of the conductances). As for single stimulation, the response was dominated by inhibition in *Stxbp1*^{wt} and by excitation in *Stxbp1*^{hap} microcircuits (Figure 5J), and the E/I ratio was increased by repetitive stimulation in the *Stxbp1*^{hap} but not in the *Stxbp1*^{wt} littermates (Figure 5K). The repetitive activation of interneurons produced a shunting inhibition that was still present 100 ms after the end of the train stimulation in *Stxbp1*^{wt} (arrows in Figure 5H) but almost absent in *Stxbp1*^{hap} microcircuits (Figure 5L).

By analyzing the relative contribution of excitatory and inhibitory synapses for these marked differences, we found that L4 to PV^+ synapses were reliable in *Stxbp1*^{wt} microcircuits because the probability for generating an action potential was still above 70% by the end of the train (Figures 6A, 6B, and 6D). Recordings obtained in voltage clamp mode revealed a short-term depression of EPSCs during the train (Figures S3E and S3G). In *Stxbp1*^{hap} microcircuits, synapses connecting L4 to PV^+ cells were far less reliable because the probability of reaching the threshold for action potentials declined rapidly and remained lower than in *Stxbp1*^{wt} microcircuits during the whole duration of the train (Figures 6C and 6D). Moreover, the short-term depression of L4 to PV^+ EPSCs was more pronounced than in *Stxbp1*^{wt} (Figures S3E–S3G). The amplitude of IPSCs evoked by intracellular current pulse injections into PV^+ neurons was declining over time (Figures 6E, 6F, and 6H). As for *Stxbp1*^{wt} microcircuits, spikes induced by current pulses in PV^+ neurons evoked IPSCs that steadily declined in amplitude (Figure 6F) with a short-term depression that was only slightly stronger than in *Stxbp1*^{hap} (Figure 6H), in agreement with previous findings obtained in cultured cells.[16]

Overall, these data demonstrate a stronger rundown of excitatory (and to a much lesser extent inhibitory) synapses within the FFI microcircuit in *Stxbp1*^{hap} animals. Strikingly, during train stimulation, inhibitory conductances almost disappeared in the *Stxbp1*^{hap}, mainly due to the failure to recruit PV^+ neurons (Figures 6C and 6D). Consequently, the "tail" of shunting inhibition at the end of the train in WT animals was absent in *Stxbp1*^{hap} (Figure 5L). This lack of post-train inhibition may open a window where the pyramidal neuron is hyperexcitable if stimulated through another excitatory input that has not experienced rundown.

Impairment of excitatory synapses leads to hyperexcitability of pyramidal neurons

To investigate whether the hyperexcitability in *Stxbp1*^{hap} microcircuits could be explained solely by the alteration of excitatory synapses, we created a mathematical model[29,30] consisting of a two-compartment pyramidal cell receiving dendritic excitatory inputs and somatic feedforward inhibitory input from several pathways at independent stochastic times (Figure 7A). The *Stxbp1*^{hap} phenotype was mimicked by decreasing the strength of excitatory synapses by 40% (i.e., a value in the range of the alterations observed for G_e; Figures 2D, 4I, and 5E) without changing inhibitory synapses. The membrane potential of the pyramidal cell was computed in response to random Poisson activation of all afferent pathways firing at 10 Hz, on average. The simulations showed that in control conditions, the excitability of pyramidal cells decreased as a function of the number of active pathways (Figures 7B and 7C), probably reflecting the relative increase in the contribution of inhibition. However, this trend was much weaker in the *Stxbp1*^{hap} model due to a lack of PV^+ recruitment with the consequence that pyramidal cells were relatively more excitable (Figures 7B and 7C). Hence, our model provides evidence that a reduction in the strength of excitatory synapses is sufficient to explain hyperexcitability as

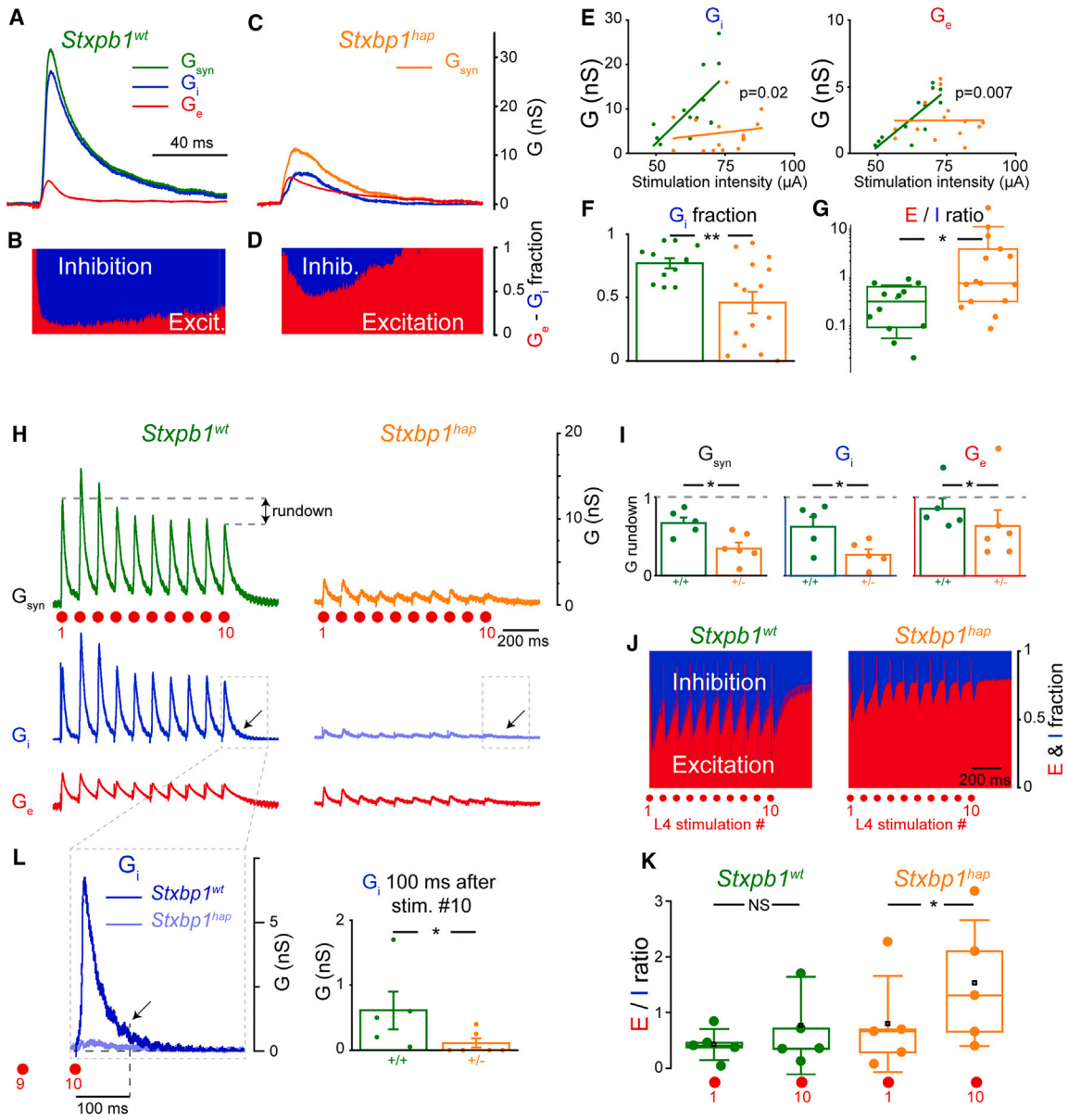

Figure 5. The ratio between inhibition and excitation is impaired in the somatosensory cortex of *Stxbp1*^{hap} animals

(A) G_{syn} (green), G_e (red), and G_i (blue) evoked by a single shock (67 μA) applied on L4 in an *Stxbp1*$^{+/+}$ animal.

(B) Fraction of excitation (G_e/G_{syn}, red) and inhibition (G_i/G_{syn}, blue).

(C and D) Same setting as in (A) and (B), but from an *Stxbp1*^{hap} animal; stimulation at 73 μA.

(E) Maximal amplitude of G_i and G_e as a function of stimulation intensity (G_i: *Stxbp1*^{wt}: 0.61 ± 0.20 nS/μA, n = 13; *Stxbp1*^{hap}: 0.07 ± 0.12 nS/μA, n = 15; p = 0.02, F test; G_e: *Stxbp1*^{wt}: 0.17 ± 0.04 nS/μA, n = 13; *Stxbp1*^{hap}: 0.00 ± 0.04 nS/μA, n = 15; p = 0.007, F test).

(F) Fraction of excitation calculated at the peak of G_{syn} (mean ± SEM for *Stxbp1*^{wt}: 0.77 ± 0.04, n = 12; *Stxbp1*^{hap}: 0.46 ± 0.09, n = 15; p = 0.007). **p < 0.01.

(G) E/I ratio (G_e/G_i) calculated at the peak of G_{syn} (*Stxbp1*^{wt}: 0.34 ± 0.08, n = 12; *Stxbp1*^{hap}: 3.56 ± 1.69, n = 15; p = 0.01). *p > 0.05.

(H) G_{syn} in an L2/3 pyramidal cell during repetitive stimulation (10 shocks at 65 μA for *Stxbp1*$^{+/+}$ and 70 μA for the *Stxbp1*^{hap} applied at 10 Hz) in an *Stxbp1*^{wt} and *Stxbp1*^{hap} animal. G_i and G_e calculated as in Figure 5A. The gray dashed lines illustrate the rundown observed between the 1st and 10th stimulations.

(I) Rundown of G_{syn}, G_i, and G_e calculated as the amplitude of the last conductance peak related to the first. Rundown of G_{syn}: mean ± SEM for *Stxbp1*^{wt} 0.67 ± 0.16 (n = 5), *Stxbp1*^{hap} 0.34 ± 0.18 (n = 6), significant difference (p = 0.02). Rundown of G_i: *Stxbp1*^{wt} 0.62 ± 0.28 (n = 5), *Stxbp1*^{hap} 0.26 ± 0.17 (n = 6), significant difference (p = 0.03). Rundown of G_e: *Stxbp1*^{wt} 0.85 ± 0.30 (n = 5), *Stxbp1*^{hap} 0.63 ± 0.49 (n = 6), significant difference (p = 0.04). *p > 0.05.

(J) Fraction of excitation and inhibition during repetitive firing (average of all of the examples; n = 5 for *Stxbp1*^{wt}, n = 6 for *Stxbp1*^{hap}).

(K) E/I ratio calculated at the peak of G_{syn} after the 1st and the 10th shock. No significant change for *Stxbp1*^{wt}: 1st: 0.43 ± 0.13; 10th: 0.61 ± 0.24, n = 5, p = 0.22. Significant increase for *Stxbp1*^{hap}: 1st: 0.76 ± 0.33; 10th: 1.54 ± 0.50, n = 5, p = 0.03).

(L) G_i increase induced by the 10th shock. Plot: mean amplitude ± SEM of G_i 100 ms after the 10th shock (indicated by the arrow): *Stxbp1*^{wt} 0.61 ± 0.3 nS (n = 5), *Stxbp1*^{hap} 0.10 ± 0.07 nS (n = 6), p = 0.02. *p < 0.05.

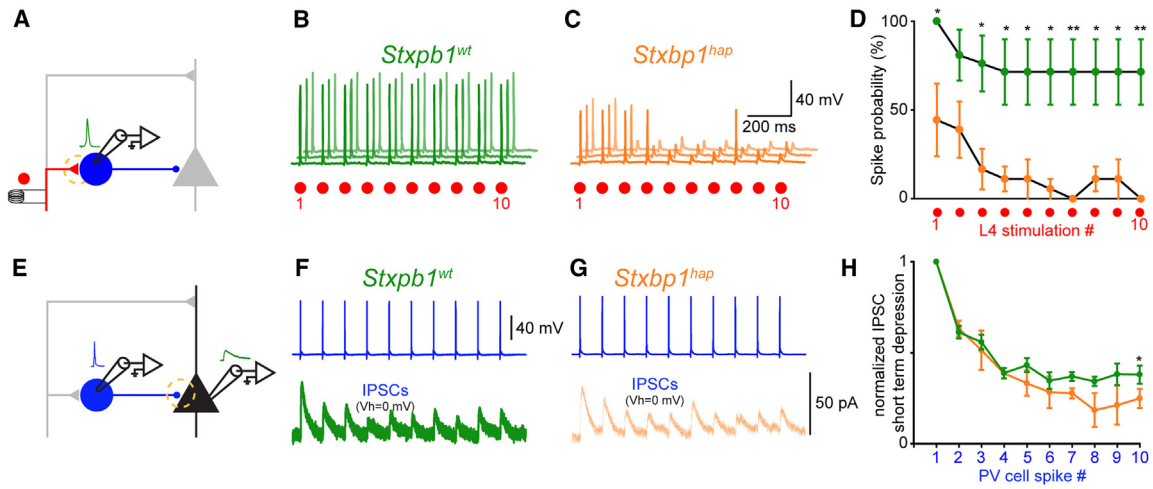

Figure 6. The short-term depression of excitatory synapses during repetitive firing reduces the recruitment of PV⁺ interneurons

(A) Schema of the experimental protocol.

(B) Response of a PV⁺ neuron from an *Stxbp1*^{wt} animal to L4 stimulation at 62 μA. Each shock induced an action potential (3 superimposed sweeps, shifted to improve the visibility).

(C) Same as in (B) from an *Stxbp1*^{hap} animal. Stimulation at 77 μA. The firing probability gradually declined.

(D) The firing probability of PV⁺ cells declined faster in *Stxbp1*^{hap} animals. Plot of the mean ± SEM of all of the PV⁺ cells tested (n = 6 for each genotype). *p < 0.05; **p < 0.01.

(E) Schema of the experimental protocol.

(F) Simultaneous recording of a PV⁺ neuron and of a connected pyramidal cell from a *Stxbp1*^{wt} animal (average of 5 consecutive sweeps). Action potentials induced in PV⁺ neurons evoked IPSCs that gradually declined (V_h = 0 mV).

(G) Same as in (F), from an *Stxbp1*^{hap} animal.

(H) Plot of the mean ± SEM of the relative amplitude of IPSCs evoked by 10 action potentials in PV⁺ interneurons. The short-term depression was slightly more pronounced for *Stxbp1*^{hap} animals (n = 6 for each genotype). *p < 0.05.

observed in *Stxbp1*^{hap} animals. Note that we did not include the stronger rundown of inhibitory synapses in *Stxbp1*^{hap} animals in the model (Figure 5H); this would further exacerbate hyperexcitability at high stimulation frequencies.

We next searched for a stimulation protocol that would directly uncover the hyperexcitability of pyramidal neurons in *Stxbp1*^{hap} animals. Based on the modeling results, we predicted that stimulating two different inputs would be key to demonstrating this phenotype. We therefore stimulated two independent sets of L4 afferents (Figure S6) that elicited EPSPs in the same L2/3 pyramidal cell, a conditioning train of 10 shocks at 10 Hz on the first pathway and test stimuli on the second (inset in Figure 7D). The independence of the pathways was demonstrated by unchanged amplitude of EPSCs elicited by the test pulse before and after the 10-Hz conditioning train (Figures S6A–S6D). We measured how the conditioning stimulation affected the probability of action potentials evoked by a test stimulation applied 100 ms after the train (Figure 7D). In control microcircuits (*Stxbp1*^{wt}), the overall excitability of pyramidal cells remained unchanged, as demonstrated by a similar firing probability before and after the train (Figures 7D and 7E). In contrast, in *Stxbp1*^{hap} microcircuits, the conditioning train produced an increase in the firing probability of pyramidal cells upon stimulation with the test pulse (Figures 7F and 7G). This directly demonstrates the hyperexcitability phenotype.

Because failure of excitatory synapses was the dominating phenotype in *Stxbp1*^{hap} animals, we predicted that a selective enhancement of excitatory synapses could rescue the hyperexcitability in *Stxbp1*^{hap} microcircuits. To test this hypothesis, we added the AMPA receptor–positive allosteric modulator (ampakine) CX516, which slows down the deactivation of the receptor upon activation by glutamate,[31,32] resulting in a strengthening of excitatory neurotransmission (Figures S6E and S6F). As expected, CX516 increased the amplitude of L4-evoked EPSPs both in PV⁺ cells (Figure 7J) and pyramidal neurons (Figure 7K). In addition, CX516 eliminated the increase in firing probability caused by the conditioning train in *Stxbp1*^{hap}, effectively reversing the situation to that of *Stxbp1*^{wt} animals (Figures 7H and 7I). This finding confirms the striking result that impaired excitation by glutamatergic afferents causes microcircuit failure in the *STXBP1* encephalopathy mouse model and that hyperexcitability can be suppressed by selectively enhancing excitatory neurotransmission.

DISCUSSION

FFI is a robust microcircuit motif that stabilizes the E/I ratio during computations performed in most of the regions of the CNS,[22,24,25] partly by setting the amplitude of EPSPs (Figure 1H) and partly by generating a time window, where integration can take place.[25] Here, we show that impaired excitatory neurotransmission in *Stxbp1*^{hap} microcircuits, when filtered through the FFI microcircuit, results in a paradoxical increase in the overall E/I ratio, which translates to hyperexcitability when considering multiple inputs. Indeed, after a single shock to L4 afferents, under conditions in which PV⁺-pyramidal GABAergic transmission is

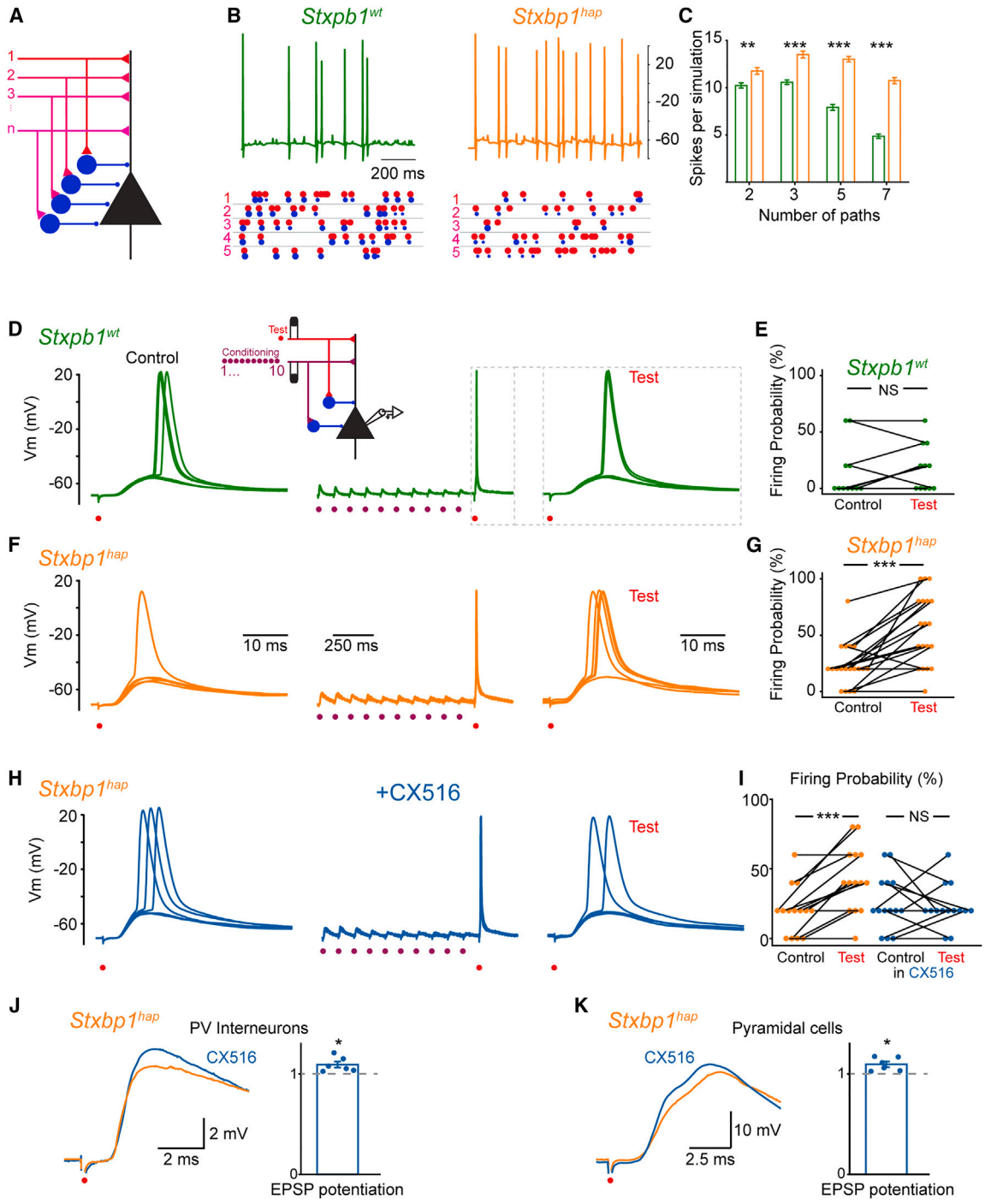

Figure 7. The impairment of excitatory synapses is responsible for the hyperexcitability of pyramidal neurons

(A) Simplified illustration of the model. A two-compartment pyramidal cell consisting of an apical dendrite and a soma receives dendritic excitatory input and somatic feedforward inhibitory input from several pathways. Each interneuron represents 5 interneurons in the model. Mutant and WT differ in the strength of excitatory synapses (40% weaker in mutant).

(B) Example of membrane potential of pyramidal cells obtained in the model in response to the simulation of random spike trains in 5 independent paths. The spikes of each pathway followed a Poisson distribution with a mean firing frequency of 10 Hz (red dots). Blue dots indicate the firing of PV^+ cells. The size of the dots is proportional to the number of PV^+ cells that fire.

(C) Average number of action potentials ± SEM in the pyramidal cell per simulation lasting 1 s, as a function of the number of pathways. Each average is based on 100 simulations. **$p < 0.01$; ***$p > 0.001$.

(legend continued on next page)

intact, the reduction in excitatory drive to PV$^+$ neurons causes a failure in PV$^+$ neuron recruitment, which suffices to increase the E/I ratio. Under repetitive stimulation of a single set of afferents, marginal increased rundown of inhibitory synapses in the *Stxbp1*^{hap} (Figures 6F–6H) further exacerbates this shift in the E/I ratio. Thus, the FFI microcircuit architecture essentially dictates that, at least in a certain area of parameter space, deficits in either excitatory or inhibitory synaptic transmissions combine to result in an increased E/I ratio, with excitatory and inhibitory defects acting synergistically. Together with the key role that FFI microcircuits play in information transfer, this may explain why a variety of psychiatric diagnoses are associated with an increased rather than a decreased E/I ratio. This is the case for autism spectrum disorders, which were hypothesized to involve an increased E/I ratio.[33] This has since been verified in animal model studies.[26,34,35] Notably, autism is a comorbidity of *STXBP1* encephalopathy and was reported in 25 of 147 affected individuals.[7] Also, schizophrenia is often assumed to imply increases in the E/I ratio, especially in the prefrontal cortex,[36] which is linked to defects in PV$^+$ interneurons.[37] Another reason for the prevalence of E/I ratio increases was pointed out by Antoine et al., who studied four mouse models of autism, all with increased E/I ratios. The authors concluded that when overall synaptic strength is reduced, increases in E/I ratios are needed to keep the synaptic depolarization and spiking in pyramidal neurons unchanged.[26] Thus, increases in the E/I ratio may be compensatory rather than causative for autism. However, epilepsy is a frequent comorbidity of autism[38]; it is therefore possible that under certain stimulation paradigms, the increase in E/I ratio, whether primary or compensatory, will lead to hyperexcitation. In the *Stxbp1*^{hap} mouse, distributing stimulations between multiple inputs revealed a hyperexcitable phenotype in the pyramidal neurons.

Some types of absence epilepsy are thought to involve the loss of FFI via inhibitory reticular neurons onto excitatory thalamic-cortical relay cells,[23] leading to thalamocortical oscillations. This has been studied in *stargazer*[39] and *Gria4*[23,40] (AMPA receptor subunits), as well as *Cacnb4* and *Cacna1a* (voltage-gated calcium channels)[41] mutant mice, all of which display impaired excitatory and unchanged inhibitory neurotransmission. In *stargazer* mice, the impairment selectively affects the expression of AMPA receptors in the dendrites of PV$^+$ interneurons.[42] *Stxbp1*^{hap} mice also display absence epilepsy, which in this case has been linked to reduced excitatory drive to fast-spiking interneurons in the striatum.[18] Miyamoto et al. showed that injection of the ampakine CX516 intraperitoneally or into the caudate putamen alleviated spike-wave discharges in *Stxbp1*^{hap} mice,[17] which are a hallmark of absence epilepsy. Impaired recruitment of PV$^+$ interneurons and their rescue by CX516 is likely at the center of this effect. Our work has dissected how this mechanism is involved in a failure to recruit cortical FFIs, which leads to cortical hyperexcitability. It should be noted that the connection between cortical hyperexcitability and epileptogenesis is complex,[43,44] and in *STXBP1* encephalopathy, epilepsy occurs as part of a pervasive neurodevelopmental disorder.[7] It is likely that impaired cortical FFI networks are involved in many symptoms of *STXBP1* encephalopathy, including intellectual disability and movement disorder.

Our finding that the synaptic strength between PV$^+$ interneurons and cortical L2/3 pyramidal neurons was unchanged or slightly increased in *Stxbp1*^{hap} animals when stimulated by single shocks appears to conflict with the observation of Chen et al.,[19] who reported reduced unitary IPSC amplitude between PV$^+$ neurons and pyramidal neurons in *Stxbp1*^{hap} mice. A possible explanation for this difference could be a gradual alteration of inhibitory synapses occurring at late developmental stages. The mice used by Chen et al.[19] were older (7–10 weeks) than the one used in the study (postnatal days 15–22). Any defect in PV$^+$-pyramidal neurotransmission adds to the deficits in excitatory drive identified here to exacerbate hyperexcitability. Interestingly, a recent study performed on a human *in vitro* model of STXBP1 encephalopathy found that knocking down STXBP1 induced a strong reduction in excitatory synaptic terminals concomitant with an increase in the strength of GABAergic synapses.[45] In agreement with our results (Figures 3 and S4), this observation suggests that the mutation induces a compensatory mechanism that is selective for inhibition.

The generation by two different groups of an *Stxbp1* haploinsufficiency condition specifically in GABAergic neurons produced different conclusions when crossing a conditional *Stxbp1* mouse line with a *Vgat*-Cre driver line[17,18] or a *GAD2*-Cre line.[11] *GAD2-Stxbp1*$^{Cre/+}$ mice died prematurely and displayed strong

(D) Left: current clamp recording of an L2/3 pyramidal cell of the somatosensory cortex from an *Stxbp1*^{wt} animal in response to a single stimulation applied in L4. Stimulation intensity adjusted to 80% of the threshold for action potentials. Center: response of the same cell during a conditioning train and a test stimulation. Inset: schema of the experimental protocol. L4 excitatory inputs stimulated with 2 bipolar electrodes. L2/L3 pyramidal cell recorded with whole-cell patch-clamp technique.

(E) The firing probability of pyramidal cells was not modified by the conditioning train (mean control: 15% ± 7%, test: 16% ± 6%, n = 11 trials from 5 cells with intensities ranging from 70% to 85% of spike threshold; firing probability calculated by the response to 5 consecutive trials; p = 0.68).

(F) Same as in (D) from an *Stxbp1*^{hap} animal.

(G) The firing probability of pyramidal cells was significantly increased by the conditioning train (mean control ± SEM: 23% ± 4%, test: 55% ± 7%, n = 19 trials from 8 cells with intensities ranging from 70% to 85% of the spike threshold; p = 0.0002). ***p < 0.001.

(H) Same cell as in (F), after addition of the ampakine CX516 (30 μM).

(I) The firing probability of pyramidal cells was not increased any more by the conditioning train. Mean firing probability ± SEM in control medium: mean control: 20% ± 5%, test: 43% ± 6%, n = 14 trials from 6 cells; p = 0.001. After the addition of CX516 on the same cells: mean firing probability: mean control: 26% ± 5%, test: 23% ± 4%, n = 14 trials from 6 cells; p = 0.79. ***p < 0.001; NS, nonsignificant.

(J) Example of EPSP recorded in a PV$^+$ cell from an *Stxbp1*^{hap} animal before (orange) and after the addition of CX516 (blue). Plot: mean potentiation of EPSPs ± SEM by CX516: from 4.7 ± 1.0 to 5.1 ± 1.0 mV (n = 6; p = 0.03. *p < 0.05.

(K) Example of EPSP recorded in a pyramidal cell from an *Stxbp1*^{hap} animal before (orange) and after the addition of CX516 (blue). Plot: mean potentiation of EPSPs ± SEM by CX516: from 20.2 ± 1.4 to 22.0 ± 1.4 mV (n = 6; p = 0.03). *p < 0.05.

epileptiform activity on electrocorticograms (ECoGs),[11] whereas *Vgat-Stxbp1*$^{fl/+}$ mice displayed normal survival, growth, and locomotor function[17] and occasional twitches and jumps coinciding with ECoG^{+} deflections but without spike-wave discharges or epileptic phenotypes.[18] This difference may be due to the fact the *Vgat* is expressed later in development than *GAD2*. The current data also revealed no major GABAergic deficits for *STXBP1* haploinsufficiency in PV^{+} neurons, although a stronger rundown was observed upon repetitive stimulation (Figure 6H), as was also observed in cultured GABAergic neurons.[16] Furthermore, other GABAergic subpopulations may be affected by *STXBP1* haploinsufficiency, as demonstrated for somatostatin-positive interneurons.[19] It was recently shown in *Drosophila* that Unc18 (the invertebrate equivalent of Munc18-1) is essential for presynaptic homeostatic plasticity.[27] Hence, it remains hard to extrapolate conclusions from animal models in which gene expression is perturbed only in specific neuron populations given the fact that homeostatic mechanisms are expected to execute radically different effects in biased versus overall perturbations. Hence, mice displaying STXBP1 haploinsufficiency specifically in GABAergic neurons are not necessarily informative for the phenotype of global *Stxbp1*^{hap} animals.

Conclusions

Attempts to rescue the consequences of *STXBP1* haploinsufficiency have so far involved compensation for the molecular deficiency (i.e., the lowered STXBP1 expression level). One strategy is to use chemical chaperones, which bind to and stabilize mutant STXBP1, thereby increasing expression levels.[10,46] Other attempts could make use of overexpression of a transgene or RNA technology to increase expression from the other, normal allele. Our study, together with previous data showing that the ampakine CX516 is effective against both absence epilepsy[18] and aggression[17] in mouse models of *STXBP1* encephalopathy indicates that potentiation of excitatory synaptic drive may be a promising treatment avenue.

Limitations of the study

Here, we studied the consequences of synaptic defect for cortical FFI in detail. Although significant for modulating the excitability of pyramidal cells, we did not investigate the role of other interneurons subtypes. Among them, somatostatin-positive interneurons (SSTs) ensure reliable inhibitory synapses onto dendrites of neighboring pyramidal neurons during high levels of activity,[47,48] including epileptiform discharges.[49] Because the connectivity between SSTs and pyramidal neurons is altered in STXBP1 encephalopathy,[19] future studies aiming at dissecting the deficiencies of SST-containing microcircuits are highly relevant.

STAR★METHODS

Detailed methods are provided in the online version of this paper and include the following:

SUPPLEMENTAL INFORMATION

Supplemental information can be found online at https://doi.org/10.1016/j.xcrm.2023.101308.

ACKNOWLEDGMENTS

We thank Anne Marie Nordvig Petersen for her excellent technical assistance. The project was funded by a Large Thematic Project grant awarded by the Lundbeck Foundation (R277-2018-802 to J.B.S., M.V., and J.F.P.) and a scholarship awarded by the Danish Research Council (to L.G.).

AUTHOR CONTRIBUTIONS

J.-F.P., M.V., and J.B.S. conceived the study and designed the experiments. A.B.S. performed, collected, and analyzed the electrophysiology data. P.B. performed the western blot. L.G., J.B.S., M.V., and J.-F.P. designed the genetically modified animals expressing TDtomato and in PV^{+} cells. L.G. maintained the colony. S.D.L. created the model and performed the simulations. A.M. wrote the Python script for analyzing the synaptic conductances. J.-F.P. wrote the original draft of the manuscript. A.B.S., M.V., and J.B.S. contributed to editing subsequent drafts. All of the authors discussed the results and commented on the manuscript.

DECLARATION OF INTERESTS

The authors declare no competing interests.

INCLUSION AND DIVERSITY

We support inclusive, diverse, and equitable conduct of research.

Received: February 17, 2023
Revised: August 29, 2023
Accepted: November 9, 2023
Published: December 11, 2023

REFERENCES

1. Catterall, W.A. (2018). Dravet Syndrome: A Sodium Channel Interneuronopathy. Curr. Opin. Physiol. *2*, 42–50.
2. Epi4K Consortium; Epilepsy Phenome/Genome Project; Allen, A.S., Berkovic, S.F., Cossette, P., Delanty, N., Dlugos, D., Eichler, E.E., Epstein, M.P., Glauser, T., et al. (2013). De novo mutations in epileptic encephalopathies. Nature *501*, 217–221.
3. EuroEPINOMICS-RES Consortium Electronic address euroepinomics-RES@uaacbe; Epilepsy Phenome/Genome Project; Epi4K Consortium; EuroEPINOMICS-RES Consortium (2017). De Novo Mutations in Synaptic Transmission Genes Including DNM1 Cause Epileptic Encephalopathies. Am. J. Hum. Genet. *100*, 179.

4. Rizo, J. (2022). Molecular Mechanisms Underlying Neurotransmitter Release. Annu. Rev. Biophys. *51*, 377–408.

5. Zhang, Y., and Hughson, F.M. (2021). Chaperoning SNARE Folding and Assembly. Annu. Rev. Biochem. *90*, 581–603.

6. Verhage, M., Maia, A.S., Plomp, J.J., Brussaard, A.B., Heeroma, J.H., Vermeer, H., Toonen, R.F., Hammer, R.E., van den Berg, T.K., Missler, M., et al. (2000). Synaptic assembly of the brain in the absence of neurotransmitter secretion. Science *287*, 864–869.

7. Stamberger, H., Nikanorova, M., Willemsen, M.H., Accorsi, P., Angriman, M., Baier, H., Benkel-Herrenbrueck, I., Benoit, V., Budetta, M., Caliebe, A., et al. (2016). STXBP1 encephalopathy: A neurodevelopmental disorder including epilepsy. Neurology *86*, 954–962.

8. Stamberger, H., Crosiers, D., Balagura, G., Bonardi, C.M., Basu, A., Cantalupo, G., Chiesa, V., Christensen, J., Dalla Bernardina, B., Ellis, C.A., et al. (2022). Natural History Study of STXBP1-Developmental and Epileptic Encephalopathy Into Adulthood. Neurology *99*, e221–e233.

9. Xian, J., Parthasarathy, S., Ruggiero, S.M., Balagura, G., Fitch, E., Helbig, K., Gan, J., Ganesan, S., Kaufman, M.C., Ellis, C.A., et al. (2022). Assessing the landscape of STXBP1-related disorders in 534 individuals. Brain *145*, 1668–1683.

10. Guiberson, N.G.L., Pineda, A., Abramov, D., Kharel, P., Carnazza, K.E., Wragg, R.T., Dittman, J.S., and Burré, J. (2018). Mechanism-based rescue of Munc18-1 dysfunction in varied encephalopathies by chemical chaperones. Nat. Commun. *9*, 3986.

11. Kovacevic, J., Maroteaux, G., Schut, D., Loos, M., Dubey, M., Pitsch, J., Remmelink, E., Koopmans, B., Crowley, J., Cornelisse, L.N., et al. (2018). Protein instability, haploinsufficiency, and cortical hyper-excitability underlie STXBP1 encephalopathy. Brain *141*, 1350–1374.

12. Martin, S., Papadopulos, A., Tomatis, V.M., Sierecki, E., Malintan, N.T., Gormal, R.S., Giles, N., Johnston, W.A., Alexandrov, K., Gambin, Y., et al. (2014). Increased polyubiquitination and proteasomal degradation of a Munc18-1 disease-linked mutant causes temperature-sensitive defect in exocytosis. Cell Rep. *9*, 206–218.

13. Saitsu, H., Kato, M., and Matsumoto, N. (2012). Haploinsufficiency of STXBP1 and Ohtahara syndrome. In Jasper's Basic Mechanisms of the Epilepsies, J.L. Noebels, M. Avoli, M.A. Rogawski, R.W. Olsen, and A.V. Delgado-Escueta, eds.

14. van Berkel, A.A., Lammertse, H.C.A., Öttl, M., Koopmans, F., Misra-Isrie, M., Meijer, M., Dilena, R., van Hasselt, P.M., Engelen, M., van Haelst, M., et al. (2023). Reduced MUNC18-1 Levels, Synaptic Proteome Changes, and Altered Network Activity in STXBP1-Related Disorder Patient Neurons. Preprint at Biological Psychiatry Global Open Science.

15. Verhage, M., and Sørensen, J.B. (2020). SNAREopathies: Diversity in Mechanisms and Symptoms. Neuron *107*, 22–37.

16. Toonen, R.F.G., Wierda, K., Sons, M.S., de Wit, H., Cornelisse, L.N., Brussaard, A., Plomp, J.J., and Verhage, M. (2006). Munc18-1 expression levels control synapse recovery by regulating readily releasable pool size. Proc. Natl. Acad. Sci. USA *103*, 18332–18337.

17. Miyamoto, H., Shimohata, A., Abe, M., Abe, T., Mazaki, E., Amano, K., Suzuki, T., Tatsukawa, T., Itohara, S., Sakimura, K., and Yamakawa, K. (2017). Potentiation of excitatory synaptic transmission ameliorates aggression in mice with Stxbp1 haploinsufficiency. Hum. Mol. Genet. *26*, 4961–4974.

18. Miyamoto, H., Tatsukawa, T., Shimohata, A., Yamagata, T., Suzuki, T., Amano, K., Mazaki, E., Raveau, M., Ogiwara, I., Oba-Asaka, A., et al. (2019). Impaired cortico-striatal excitatory transmission triggers epilepsy. Nat. Commun. *10*, 1917.

19. Chen, W., Cai, Z.L., Chao, E.S., Chen, H., Longley, C.M., Hao, S., Chao, H.T., Kim, J.H., Messier, J.E., Zoghbi, H.Y., et al. (2020). Stxbp1/Munc18-1 haploinsufficiency impairs inhibition and mediates key neurological features of STXBP1 encephalopathy. Elife *9*, e48705.

20. Orock, A., Logan, S., and Deak, F. (2018). Munc18-1 haploinsufficiency impairs learning and memory by reduced synaptic vesicular release in a model of Ohtahara syndrome. Mol. Cell. Neurosci. *88*, 33–42.

21. Patzke, C., Han, Y., Covy, J., Yi, F., Maxeiner, S., Wernig, M., and Südhof, T.C. (2015). Analysis of conditional heterozygous STXBP1 mutations in human neurons. J. Clin. Invest. *125*, 3560–3571.

22. Hu, H., Gan, J., and Jonas, P. (2014). Interneurons. Fast-spiking, parvalbumin(+) GABAergic interneurons: from cellular design to microcircuit function. Science *345*, 1255263.

23. Paz, J.T., and Huguenard, J.R. (2015). Microcircuits and their interactions in epilepsy: is the focus out of focus? Nat. Neurosci. *18*, 351–359.

24. House, D.R.C., Elstrott, J., Koh, E., Chung, J., and Feldman, D.E. (2011). Parallel regulation of feedforward inhibition and excitation during whisker map plasticity. Neuron *72*, 819–831.

25. Pouille, F., and Scanziani, M. (2001). Enforcement of temporal fidelity in pyramidal cells by somatic feed-forward inhibition. Science *293*, 1159–1163.

26. Antoine, M.W., Langberg, T., Schnepel, P., and Feldman, D.E. (2019). Increased Excitation-Inhibition Ratio Stabilizes Synapse and Circuit Excitability in Four Autism Mouse Models. Neuron *101*, 648–661.e4.

27. Ortega, J.M., Genç, Ö., and Davis, G.W. (2018). Molecular mechanisms that stabilize short term synaptic plasticity during presynaptic homeostatic plasticity. Elife *7*, e40385.

28. Wilent, W.B., and Contreras, D. (2005). Dynamics of excitation and inhibition underlying stimulus selectivity in rat somatosensory cortex. Nat. Neurosci. *8*, 1364–1370.

29. Carnevale, N.T., and Hines, M.L. (2006). The Neuron Book (Cambridge University Press).

30. Sarid, L., Bruno, R., Sakmann, B., Segev, I., and Feldmeyer, D. (2007). Modeling a layer 4-to-layer 2/3 module of a single column in rat neocortex: interweaving in vitro and in vivo experimental observations. Proc. Natl. Acad. Sci. USA *104*, 16353–16358.

31. Danysz, W. (2002). CX-516 Cortex pharmaceuticals. Curr. Opin. Invest. Drugs *3*, 1081–1088.

32. Frydenvang, K., Pickering, D.S., and Kastrup, J.S. (2022). Structural basis for positive allosteric modulation of AMPA and kainate receptors. J. Physiol. *600*, 181–200.

33. Rubenstein, J.L.R., and Merzenich, M.M. (2003). Model of autism: increased ratio of excitation/inhibition in key neural systems. Gene Brain Behav. *2*, 255–267.

34. Banerjee, A., Rikhye, R.V., Breton-Provencher, V., Tang, X., Li, C., Li, K., Runyan, C.A., Fu, Z., Jaenisch, R., and Sur, M. (2016). Jointly reduced inhibition and excitation underlies circuit-wide changes in cortical processing in Rett syndrome. Proc. Natl. Acad. Sci. USA *113*, E7287–E7296.

35. Gibson, J.R., Bartley, A.F., Hays, S.A., and Huber, K.M. (2008). Imbalance of neocortical excitation and inhibition and altered UP states reflect network hyperexcitability in the mouse model of fragile X syndrome. J. Neurophysiol. *100*, 2615–2626.

36. Lisman, J. (2012). Excitation, inhibition, local oscillations, or large-scale loops: what causes the symptoms of schizophrenia? Curr. Opin. Neurobiol. *22*, 537–544.

37. Ferguson, B.R., and Gao, W.J. (2018). PV Interneurons: Critical Regulators of E/I Balance for Prefrontal Cortex-Dependent Behavior and Psychiatric Disorders. Front. Neural Circ. *12*, 37.

38. Canitano, R. (2007). Epilepsy in autism spectrum disorders. Eur. Child Adolesc. Psychiatr. *16*, 61–66.

39. Lacey, C.J., Bryant, A., Brill, J., and Huguenard, J.R. (2012). Enhanced NMDA receptor-dependent thalamic excitation and network oscillations in stargazer mice. J. Neurosci. *32*, 11067–11081.

40. Beyer, B., Deleuze, C., Letts, V.A., Mahaffey, C.L., Boumil, R.M., Lew, T.A., Huguenard, J.R., and Frankel, W.N. (2008). Absence seizures in C3H/HeJ

and knockout mice caused by mutation of the AMPA receptor subunit Gria4. Hum. Mol. Genet. *17*, 1738–1749.

41. Caddick, S.J., Wang, C., Fletcher, C.F., Jenkins, N.A., Copeland, N.G., and Hosford, D.A. (1999). Excitatory but not inhibitory synaptic transmission is reduced in lethargic (Cacnb4(lh)) and tottering (Cacna1atg) mouse thalami. J. Neurophysiol. *81*, 2066–2074.
42. Maheshwari, A., Nahm, W.K., and Noebels, J.L. (2013). Paradoxical proepileptic response to NMDA receptor blockade linked to cortical interneuron defect in stargazer mice. Front. Cell. Neurosci. *7*, 156.
43. Badawy, R.A.B., Harvey, A.S., and Macdonell, R.A.L. (2009). Cortical hyperexcitability and epileptogenesis: understanding the mechanisms of epilepsy - part 1. J. Clin. Neurosci. *16*, 355–365.
44. Badawy, R.A.B., Harvey, A.S., and Macdonell, R.A.L. (2009). Cortical hyperexcitability and epileptogenesis: Understanding the mechanisms of epilepsy - part 2. J. Clin. Neurosci. *16*, 485–500.
45. McLeod, F., Dimtsi, A., Marshall, A.C., Lewis-Smith, D., Thomas, R., Clowry, G.J., and Trevelyan, A.J. (2023). Altered synaptic connectivity in an in vitro human model of STXBP1 encephalopathy. Brain *146*, 850–857.
46. Abramov, D., Guiberson, N.G.L., Daab, A., Na, Y., Petsko, G.A., Sharma, M., and Burré, J. (2021). Targeted stabilization of Munc18-1 function via pharmacological chaperones. EMBO Mol. Med. *13*, e12354.
47. Pouille, F., and Scanziani, M. (2004). Routing of spike series by dynamic circuits in the hippocampus. Nature *429*, 717–723.
48. Silberberg, G., and Markram, H. (2007). Disynaptic inhibition between neocortical pyramidal cells mediated by Martinotti cells. Neuron *53*, 735–746.
49. Parrish, R.R., Codadu, N.K., Mackenzie-Gray Scott, C., and Trevelyan, A.J. (2019). Feedforward inhibition ahead of ictal wavefronts is provided by both parvalbumin- and somatostatin-expressing interneurons. J. Physiol. *597*, 2297–2314.

STAR★METHODS

KEY RESOURCES TABLE

REAGENT or RESOURCE	SOURCE	IDENTIFIER
Antibodies		
Goat monoclonal anti-PV	Swant	Code No. PVG-213
Donkey, monoclonal anti-goat, Alexa Fluor 647	Sigma-Aldrich	Cat# SAB4600175; RRID: AB_2650496
Rabbit Munc18-1	Sigma-Aldrich	Cat# HPA023483; RRID: AB_2734139
Goat anti-Rabbit IgG	Sigma-Aldrich	Cat# P0448; RRID: AB_258284
Actin Peroxidase Monoclonal	Abcam	Cat# A3854; RRID: AB_262011
Chemicals, peptides, and recombinant proteins		
CX516	Sigma-Aldrich	SML1191; CAS: 154235-83-3
Tetrodotoxin (TTX)	Alomone	Cat #: T-550 CAS No.: 18660-81-6
CNQX	Sigma-Aldrich	CAS Number: C127 CAS: 115066-14-3
AP5	helloBio	HB0252
QX-314	Tocris	Cat. 1014
RIPA buffer	Sigma-Aldrich	R0278
Protease inhibitor	Thermo Fisher Scientific	87786
Phosphatase inhibitor	Thermo Fisher Scientific	78420
Pierce™ BCA Protein Assay Kit	Thermo Fisher Scientific	23227
4X Bolt™ LDS Sample Buffer	Thermo Fisher Scientific	B0007
10X Bolt™ Sample Reducing Agent	Thermo Fisher Scientific	B0009
Bolt™ Bis-Tris Plus Mini Protein Gels, 4–12%	Thermo Fisher Scientific	NW04120BOX
NuPAGE™ MES SDS Running Buffer (20X)	Thermo Fisher Scientific	NP0002
PVDF membrane	Amersham	GE10600021
PageRuler™ Prestained Protein Ladder	Thermo Fisher Scientific	26616
Pierce ECL Plus kit	Thermo Fisher Scientific	32132
Sodium dodecyl sulfate solution, 10% in water	Sigma-Aldrich	71736
Trizma® base	Sigma-Aldrich	T1503
Difco™ Skim Milk	BD Life Sciences	Tween®20
Deposited data		
Model	This paper	https://modeldb.science/2014828
Script for counting TD-tomato	This paper	https://github.com/sdalumlarsen/STXBP1.
Experimental models: Organisms/strains		
C57Bl6 *Stxbp1*$^{+/-}$	described in Verhage et al.[6]	N/A
B6.129P2-*Pvalb*$^{tm1(cre)Arbr}$/*Pvalb*$^{tm1(cre)Arbr}$	The Jackson Laboratory	JAX #017320
Gt(ROSA)26Sor$^{tm1.1(CAG-tdTomato/GCaMP6f)Mdcah}$/ *Gt(ROSA)26Sor*$^{tm1.1(CAG-tdTomato/GCaMP6f)Mdcah}$	The Jackson Laboratory	JAX #031968
Software and algorithms		
Clampfit 10.7	Molecular Devices	https://support.moleculardevices.com
Python 3.7	Python Software Foundation	https://www.python.org/psf-landing/
OriginPro	OriginLab	https://www.originlab.com
Prism 7	GraphPad Software	https://www.graphpad.com/

RESOURCE AVAILABILITY

Lead contact

Further information and requests for resources should be directed to and will be fulfilled by the lead contact, Jean-François Perrier (perrier@sund.ku.dk).

Materials availability

Materials generated in this study that are not commercially available are available from the lead contact with a completed Materials Transfer Agreement.

Data and code availability

- Any data requested will be made available upon request.
- The model and relevant files are available at ModelDB, the script for counting TDtomato positive neurons and relevant files are available at GitHub and are publicly available as of the date of publication. DOIs are listed in the key resources table.
- Any additional information required to reanalyze the data reported in this work paper is available from the lead contact upon request.

EXPERIMENTAL MODEL AND SUBJECT DETAILS

Mice

All procedures were carried out according to Danish animal welfare legislation, and breeding of mice was approved by the Animal Experiments Inspectorate (2018-15-0202-00157). Mice (P15 – 22) of both sexes were used. Heterozygous C57Bl6 *Stxbp1*mice (*Stxbp1*$^{+/-}$) were crossed with wild type C57Bl6 STXBP$^{+/+}$ mice to obtain *Stxbp1*$^{+/-}$ animals and control *Stxbp1*$^{+/+}$ littermates. In the text, we refer to these mice as *Stxbp1*^{hap} (*hap* for haploinsufficiency) and *Stxbp*^{WT}, respectively. The *Stxbp1* mouse line was described before.[6] All animals were PCR genotyped before and after experiments. Animals expressing TdTomato in PV + cells were generated as follows. We created a *Stxbp1* KO line homozygous for *Pv-Cre* by interbreeding B6 *Pv-Cre*/*Pv-Cre* (B6.129P2-*Pvalb*$^{tm1(cre)Arbr}$/*Pvalb*$^{tm1(cre)Arbr}$, JAX stock #017320) and *STXBP1*$^{+/-}$. For dual patching, we crossed females *Pv-Cre*/*Pv-Cre*; *Stxbp1*$^{+/-}$ with males from a homozygous *Salsa6f* line (B6(129S4)-*Gt(ROSA)26Sor*$^{tm1.1(CAG-tdTomato/GCaMP6f)Mdcah}$/*Gt(ROSA)26Sor*$^{tm1.1(CAG-tdTomato/GCaMP6f)Mdcah}$; JAX stock #031968). The offspring was PCR genotyped to identify littermate *Pv-Cre*/-; *Salsa6f*/-; *Stxbp1*$^{+/-}$ and *Pv-Cre*/-; *Salsa6f*/-; *Stxbp1*$^{+/+}$. Validation of appropriate fluorescence expression in PV + interneurons is provided in Figure S2.

METHOD DETAILS

Immunohistochemistry

300 μm thick sagittal slices were fixed overnight in paraformaldehyde (4%) and rinsed 3 times in phosphate buffered saline (PBS). The slices were heated to 75°C for 20 min in 10 mM citrate buffer (pH = 6.0) and then rinsed 3 times in PBS. Unspecific binding sites were blocked by washing the slices in PBS/Triton/0.2% gelatine for 30 min.

A primary antibody directed against parvalbumin (Goat, Swant - Switzerland) concentration (1:1000) was applied on the slice and incubated overnight at 4°C. The slices were then rinsed 3 times in 0.3% Triton X-100/PBS and incubated for 1 h at room temperature with the secondary fluorescent antibody (Donkey, anti-goat, Alexa Fluor 647 secondary, Sigma-Aldrich - USA) concentration (1:500). The slices were then rinsed for 10 min in 0.1% Triton X-100/PBS and then twice in PBS before being mounted on a coverslip.

Confocal microscopy images were obtained at the core facility for integrated microscopy (CFIM) of the Faculty of Health and Medical Sciences of the University of Copenhagen. Pictures were taken with an LSM 900 confocal microscope (Zeiss, Germany) equipped with a Zeiss 20X/0.8 objective. Alexa Fluor 568 and 647 positive cells were excited with 555 nm and 640 nm diode lasers, respectively.

Western blot

Frozen cortices were homogenised and lysed in RIPA buffer (Sigma-Aldrich), supplemented by protease inhibitor (Thermo Fisher Scientific) and phosphatase inhibitor (Thermo Fisher Scientific), using electrical rotor and pestles. The samples were incubated on ice for 30 min, followed by 12000 g centrifugation at 4°C for 10 min. The supernatant was tipped off and protein concentrations were measured by Pierce BCA Protein Assay Kit (Thermo Fisher Scientific). The samples were prepared by mixing 20 μg proteins with LDS sample buffer (Thermo Fisher Scientific), Sample Reducing Agent (Thermo Fisher Scientific) and water, followed by 95°C incubation for 5 min. The proteins were separated by electrophoresis in 4–12% Bis-Tris Plus Gel and wet-transferred to PVDF membrane. Membranes were blocked in 5% skim milk TBS-T and blotted with primary antibody diluted in 1% skim milk TBS-T overnight at 4°C (Munc18-1 1:2000, Sigma-Aldrich HPA023483; β-Actin 1:20000, Abcam A3854). The day after, membranes were washed with TBS-T three times for 10 min each, and incubated with secondary antibody (anti-Rabbit IgG 1:10 000, Sigma-Aldrich P0448) diluted in 1% skim milk TBS-T for 1 h at room temperature. After three times of washing with TBS-T, PVDF membranes were imaged using Pierce ECL Plus kit (Thermo Fisher Scientific) in the FluorChem E system (Bio-Techne). The raw intensities of bands were measured in ImageJ and normalized to the loading control (β-Actin) for the relative intensity, and then divided by the wildtype average to calculate the fold change.

Electrophysiology

After decapitation (P15 – P22), the head was submerged in ice-cold artificial cerebrospinal fluid (aCSF; 125 mM, NaCl, 25 mM $NaHCO_3$, 1.25 mM NaH_2PO_4, 2.5 mM KCl, 0.5 mM $CaCl_2$, 7 mM $MgCl_2$, 25 mM glucose; all from Sigma-Aldrich) saturated with

carbogen. The brain was extracted, glued to a metal stage and placed in the slicing chamber filled with cool aCSF saturated with carbogen. Sagittal sections (300 μm thick) were made with a vibratome (VT1200 vibratome; Leica Biosystems, Germany) and transferred to aCSF (125 mM, NaCl, 25 mM $NaHCO_3$, 1.25 mM NaH_2PO_4, 2.5 mM KCl, 2.5 mM $CaCl_2$, 1.3 mM $MgCl_2$, 25 mM glucose; all from Sigma-Aldrich) saturated with carbogen at 28°C for 1 h. The slices were then maintained at room temperature until recording.

Brain slices were placed in a recording chamber under the objective of an upright microscope equipped with epifluorescence illumination (SliceScope Pro 1000, Scientifica Ltd, United Kingdom). The chamber was continuously perfused with aCSF saturated with carbogen. Patch electrodes (resistance of 4–7 MΩ) were pulled on a P-87 or P-1000 pipette puller (Sutter Instruments Co., USA). Pyramidal neurons and PV + interneurons from L2/3 of the somatosensory or motor cortex were recorded with the whole-cell patch clamp configuration in voltage or current-clamp mode. For voltage-clamp recordings, pipettes were filled with 110 mM Cesium methanesulfonate, 2.5 mM Na_2ATP, 2.5 mM $MgCl_2$, 2.8 mM NaCl, 20 mM HEPES, 0.4 mM EGTA, 10 mM biocytin, (all from Sigma-Aldrich), 5 nM QX-314 (helloBio) and 0.1 mM Alexa Fluor 568 or Alexa Fluor 488 hydrazide (Invitrogen; pH 7.4). For current clamp recordings, pipettes were filled with 122 mM K-gluconate, 5 mM Na_2ATP, 2.5 mM $MgCl_2$, 0.0003 mM $CaCl_2$, 5.6 mM Mg-gluconate, 5 mM K-HEPES, 5 mM HEPES, 1 mM EGTA, 10 mM biocytin (all from Sigma-Aldrich), and 0.1 mM Alexa Fluor 568 or Alexa Fluor 488 hydrazide (Invitrogen; pH 7.4). Patch pipettes were positioned on a three-axis motorised micromanipulator (PatchStar, Scientifica Ltd, United Kingdom) connected to a CV-7B Headstage (Molecular Devices, Sunnyvale CA, USA).

Recordings

Recordings were made using a MultiClamp 700B amplifier (Molecular Devices, CA, USA). Data were sampled at 20 kHz, sent to a computer via a Digidata 1550B digitizer (Molecular Devices, Sunnyvale CA, USA). Recordings of synaptic currents in pyramidal neurons from L2/3 of the somatosensory cortex were performed on Munc18-1 heterozygous mutant mice (*Stxbp1*$^{+/-}$)[6] and control littermates (*Stxbp1*$^{+/+}$). AP5 (50 μM) and CNQX (10 μM) (both from Sigma-Aldrich) was applied in the bath, when experiments where performed to confirm the stimulation of FFI circuit (Figure 1). Simultaneous recordings of PV + interneurons and connected pyramidal cells were performed on homozygous (*STXBP1*$^{+/+}$) and heterozygous mutant mice (*STXBP1*$^{+/-}$) expressing TdTomato and GCaMP6 under the parvalbumin promoter. Pyramidal neurons were identified by their shape and confirmed by intracellular staining with Alexa 488 or Alexa 568 (Invitrogen). They had a characteristic apical dendrite oriented to the surface of the cortex and basal dendrites oriented perpendicularly (Figure 1A). In few instances, pyramidal neurons were recorded in current clamp mode. All fired regularly in response to depolarizing current pulses with a maximal firing frequency of 24.6 ± 3.0 Hz (n = 6). mEPSCs and mIPSCs were recorded in 1 μM tetrodotoxin (TTX, Alamone) while holding the membrane potential at −70 and 0 mV respectively. Miniature events were handpicked and analyzed in Clampfit 10.7 (Molecular Devices, USA). Series resistance was compensated by bridge balance. Access resistance was monitored throughout the recordings. Data were excluded if the access resistance was above 30 MΩ or if changed by >20% during recording. Pyramidal cells were excluded if their membrane potential was above −55mV.

TdTomato-labelled PV + interneurons were identified by epifluorescence and recorded in whole-cell configuration in current-clamp and voltage-clamp mode. Neighbor pyramidal cells were recorded in whole-cell configuration in voltage-clamp mode kept at 0 mV. The cells were considered as synaptically connected if action potentials elicited by a 2-5ms depolarizing current pulse in PV + cells induced an IPSC with fixed latency in the pyramidal cell. The IPSC latency was defined as the time from the peak of the spike to the start of the IPSC. The slope of the IPSC was estimated from the 20–80% rise time by means of Clampfit software (Molecular Devices, CA, USA). In some instances, interneurons were recorded from slices from heterozygous mice of MUNC18-1 animals. We systematically tested their ability to fire action potentials in response to depolarizing current pulses. Neurons that could fire above 100 Hz were considered as PV + basket cells.[22]

Estimation of the number of TdTomato positive neurons in L2/3 was performed by automatic detection of regions of interest (ROIs) by a home-made script written in Python. Images were median filtered with a kernel size of 10, dynamically thresholded with a block size of 31 and an offset of −25 and then morphologically opened and closed both with a kernel size of 3. Connected regions in the resulting binary image were defined as ROIs if they contained more than 50 pixels. The transition between L1 and L2/3 was set at the center of the ROI with the lowest cortical depth. ROIs were accepted as L2/3 neurons if their cortical depth was less than 200 pixels (129μm) deeper than the L1-L2/3 transition. The script can be found at https://github.com/sdalumlarsen/STXBP1.

Stimulation

A bipolar stimulation electrode (TM33CCNON; World Precision Instruments, Sarasota, FL, USA) connected to a stimulus isolator (A365RC, WPI, UK) was positioned in L4 of the somatosensory cortex. The threshold for inducing synaptic responses was adjusted to elicit 5/5 EPSCs in the recorded pyramidal cell, as in other works.[24] For few experiments, minimal stimulation intensities sufficient to induce at least one response (or failures) were applied (Figures S1C and S1D). They are referred to as minimal stimulation. For dual stimulation, two electrodes were positioned in L4, on each side of the L2/3 recorded pyramidal cell. The distance between stimulation electrodes ranged from 200 to 300 μm. For excitability tests (Figure 8), the firing probability was quantified in comparison to the minimal intensity necessary for inducing 5/5 action potentials in the pyramidal neurons. Conditioning trains (10 shocks, 10 Hz) were applied at 1.2 times the minimal intensity for inducing 5/5 EPSCs. CX516 (30μM, Sigma-Aldrich) was bath applied to prevent the hyperexcitability (Figure 8).

QUANTIFICATION AND STATISTICAL ANALYSIS

Data analysis

Data analysis was performed using Clampfit 10.7 (Molecular Devices, USA), Python 3.7 (Python Software Foundation), OriginPro 2017 (OriginLab, USA). Statistics were done with Prism 7 (GraphPad Software, USA) and OriginPro 2017 (OriginLab, USA). Samples were compared with the unpaired Mann–Whitney U test, and paired Wilcox matched-pairs. Slopes of linear regressions were compared with the F-test. Data are presented as mean ± standard error of the mean (SEM) or standard deviation of the mean (SD) when specified. Significance was designated as follows: *$p < 0.05$; **$p < 0.01$; ***$p < 0.001$.